Squaramide-based interpenetrated networks for load-bearing applications

Chen, Y.

Chapter 2

Modulation of Thermally Driven Transitions in Squaramide-based Supramolecular Hydrogels

Temperature is a potent stimulus that can build and transform supramolecular materials from the molecular to the macroscopic scales. In this work, we designed a small library of squaramide-based monomers to delineate the structural modifications necessary to tune the formation of fibrillar aggregates and gel phase materials that respond to temperature. We found that the substitution of carbamate linkages with an ether bonds results in the formation of a 4-fold less stiff hydrogel relative to the native tripodal squaramide monomer, whereas a hydrogel still form at high concentrations even when lacking a squaramide moiety. Importantly, these structural modifications alter the response of the gels to temperature. After heating to 130°C and cooling them back to room temperature, we observed that hydrogels composed of molecules with symmetrical tripodal squaramide-based structures can retain their original shapes as gels but underwent shrinkage, eventually transforming into materials with a high degree of internal order. Understanding the effect of temperature on supramolecular hydrogels constructed from small molecule monomers opens the door to a range of applications in the biomedical field.

This chapter was prepared as a research article: Ying Chen, Francesca Lauria, Thomas J.F. Kock, Goutam Ghosh, Marco M. R. M. Hendrix, Ilja K. Voets, Gustavo Fernandez, Roxanne E. Kieltyka*

2.1 Introduction

Supramolecular polymers have sparked much interest for their unique properties that arise from the inherent dynamic character of the interactions that hold them together.[1-5] The delicate balance of noncovalent interactions, such as hydrogen bonding, hydrophobic-hydrophilic interactions, van der Waals forces, and π-π interactions in the monomer, permit tuning of their structural and functional of the resultant polymers and materials. As hydrogels, altering their molecular structures opens the door to tune their mechanics and responsiveness to a diverse range of physical and chemical stimuli.[4,6,7] However, the rational design of supramolecular materials starting from small molecule monomers and prediction of their final properties and behaviours remains challenging. This holds especially in water, where the hydrophobic effect has a major influence on supramolecular polymerization and hydrogelation process, and ultimately their final properties, such as their mechanics and thermoreponsiveness.[8-12]

Thermo-responsive polymers are being extensively investigated due to their broad applicability for use in the biomedical field (e.g., drug delivery, sensors and tissue engineering) that comes from their capacity to undergo physical changes in response to temperature.[13-17] There is a particular interest in exploring the lower critical solution temperature (LCST), where a distinct phase shift occurs due to dehydration of the polymer chains above a given temperature, in such materials. To access this property in the supramolecular materials, an often used strategy involves the tethering of molecular recognition units to water soluble polymers that exhibit this behaviour.[18,19] Moreover, filamentous supramolecular polymers that are constructed from the assembly of small molecule monomers respond distinctly to temperature in line with their specific chemistries. For example, in peptide-based systems often disruption of the assemblies is observed with increasing temperature leading to gel-to-sol transitions whereas in small molecule monomers with oligo(ethylene glycol) chains LCST behaviour can be detected within the assemblies. In these monomers, the hydrophobic core of the gelator remains shielded from water maintaining the assembly, while the hydrophilic part (e.g., oligoethylene glycol) that is thermo-responsive enables nanophase segregation and further regulates material properties.[24,25] Therefore, balancing hydrophobicity with the appropriate hydrogen bond design and the hydrophilic peripheral parts that interact with water molecules is critical to facilitate thermo-responsive behavior.[20-23]

We previously reported a tripodal squaramide-based monomer capable of self-assembling into supramolecular polymers and forming gel-phase materials in water.[34] In a first approach, we varied the aliphatic chain length (ranging from 6 to 12 methylene units) in the hydrophobic region of a tripodal amphiphile, resulting in hydrogel materials for 8 to 10 carbons whereas highlighting the importance of hydrogen bonding and a balance of the hydrophilic and hydrophobic domains on the gelation of the monomer. Inspired by these results, we designed a library of tripodal squaramide-based monomers to further understand the impact of a range of chemical modifications to the tripodal squaramide-based gelator evaluating their mechanics and thermal behaviour in the assembled state. It was envisaged that the non-uniform changes to the monomer geometry and hydrophobic content, as well as the number of squaramides and the presence of the carbamate moiety, will affect the supramolecular polymerization, gelation, and thermo-responsive properties in aqueous solution.

2.2 Result and Discussion

Tripodal Squaramide-Based Amphiphile Design and Synthesis

We sought first to understand the features (e.g., hydrophilicity, hydrogen bonds, etc.) of the tripodal squaramide-based monomers that enable them to form supramolecular hydrogels and the tuning of their physical properties (Scheme 1, Figure S1-S5).[18] We synthesized **5** according to an earlier method reported by our group[18] and evaluated the influence of the carbamate moiety in **5** by preparing **4** with an ether moiety.[19] We first conjugated tetraethylene glycol monomethyl ether and 1,10-dibromodecane in the presence of sodium hydride. We then converted the resultant amphiphilic monomer that containing a halide into a primary amine by the Gabriel synthesis and coupled 3,4-dibutoxy-3-cyclobutene-1,2-dione to obtain the squaramide-based amphiphile. In the last step, we reacted tris(2-aminoethylamine) (TREN) with the squaramide amphiphile to obtain the final tripodal supramolecular monomer **4**.

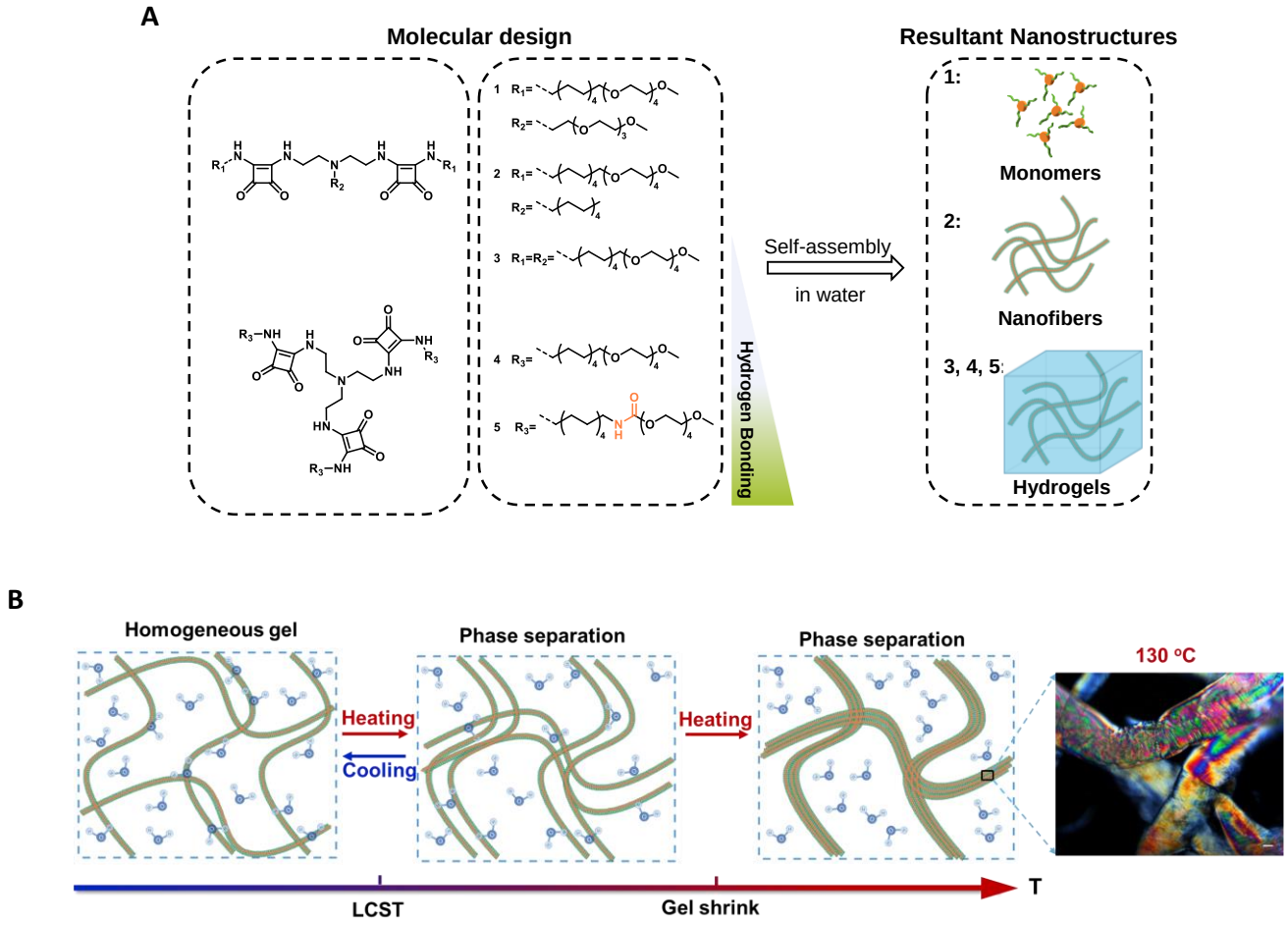

Scheme 1. (A) Squaramide-based tripodal supramolecular monomers **1**-**5** used in this study, and their self-assembly into supramolecular polymers and gel-phase materials. (B) Schematic of thermal transitions in the supramolecular network of **4** with increasing temperature.

We further explored a second set of monomers (**1**-**3**) to understand the effect of reducing the number of squaramide moieties and modifying the hydrophilic-hydrophobic balance within the monomer. We implemented this alteration to investigate the impact of aliphatic spacers linked to the oligo(ethylene glycol) chains and the carbamate bonds on the supramolecular polymerization of squaramide moieties. Monomers **1**-**3** consisted of two squaramide amphiphiles arms that contain ester bonds like **4**, and we coupled a third arm with either an oligoethylene glycol chain (**1**, ωTEG = 0.55), a

shorter alkyl chain (**2**, ωTEG = 0.53), or a chain consisting of alkyl and oligoethylene glycol segments (**3**, ωTEG = 0.46) directly attached to the nitrogen of the TREN core (Scheme S1). We synthesized monomers **1**-**3** starting from reacting benzyl alcohol with diethylenetriamine to obtain N,N″-di-Z-diethylenetriamine followed by coupling of oligoethylene glycol (**12a**), a short alkyl chain (**12b**) or a chain with alkyl and oligoethylene glycol domains (**12c**) onto the N,N'-di-Z-diethylenetriamine core. After in situ catalytic hydrogenation with triethylsilane and palladium on carbon to remove the carboxybenzyl-protecting group, the core was further coupled with two squaramide-based amphiphiles (**9**) to obtain the monomers **1**-**3**.

Evaluation of supramolecular polymer and gel properties at ambient temperature

We first investigated the ability of the tripodal squaramide-based monomers **1**-**5** to form gels in water by the gel inversion method and oscillatory rheology. Sonication of the various monomers in water led to gels for monomers **3** – **5** (Figure S6-S9). Monomer **5**[18] exhibited a critical gelation concentration (CGC) of 1.5-2 mM, whereas **4** containing the ester moiety showed a higher CGC of 2-2.5 mM consistent with the formation of fewer hydrogen bonds (Figure S8-S9). Further removal of one of the squaramide moieties in **3** showed an even higher CGC value (4-5 mM) and longer gelation time (Figure S7). These results suggest that both the importance of the number of hydrogen bonds both in the core and on the periphery of the amphiphile to tune the hydrogel storage modulus. Further removal of the alkyl chain from **3** leaving only an oligoethylene glycol chain (**1**) resulted in excellent water solubility with no gel being formed up to 6 mM. In contrast, exchange of one of the amphiphile arms for a hydrophobic group as in **2** resulted in visible precipitation at concentrations as low as 0.75 mM (Figure S6).

We then quantified the mechanical properties of hydrogels **3** - **5** by oscillatory rheology to understand the impact of the various structural substitutions of the hydrogelators (Figure 1A-C, S10-S11). We performed time sweep measurements on the hydrogels to gain insight into the time for the hydrogels to recover after their dispensing on the rheometer plate and to understand if their properties continue to change over time. We then determined the linear viscoelastic regime (LVE) of the hydrogels though an amplitude sweep measurement. Hydrogel **5** (5 mM) exhibited constant storage (G') and loss (G'') moduli until 3% strain, while hydrogels **3** (5 mM) and **4** (5 mM) showed less brittle behaviour showing constant moduli until strains of 10% and 7%, respectively. Frequency sweep experiments showed that hydrogels **4** and **5** exhibited a G' nearly 10 times higher than the G'' and showed frequency independent behavior within the measured range and more elastic character. Conversely, hydrogel **3** displayed a G' only 2 times higher than G'' and showed weak frequency dependence, suggestive of more viscoelastic behavior. More specifically, hydrogel **5** showed the greatest storage modulus of 100 Pa whereas **4** and **5** showed a significant decrease to 19 and 8 Pa, respectively, consistent with a decrease in the number of hydrogen bonds that can be formed between the various monomers. Because of the supramolecular nature of the gels, we evaluated their capacity to self-recover by performing a step-strain test. Here, a large strain outside the LVE is applied to the supramolecular hydrogel and then removed evaluating its response throughout the process. Subjecting the hydrogels to a large amplitude strain (300%) resulted in a decrease of the G' values of **3**-**5** with an inversion of their moduli (G'' > G'). Withdrawal of the large amplitude strain, all hydrogels formed gels again (G' > G'') though with a slight decrease in G' to a similar extent between monomers.

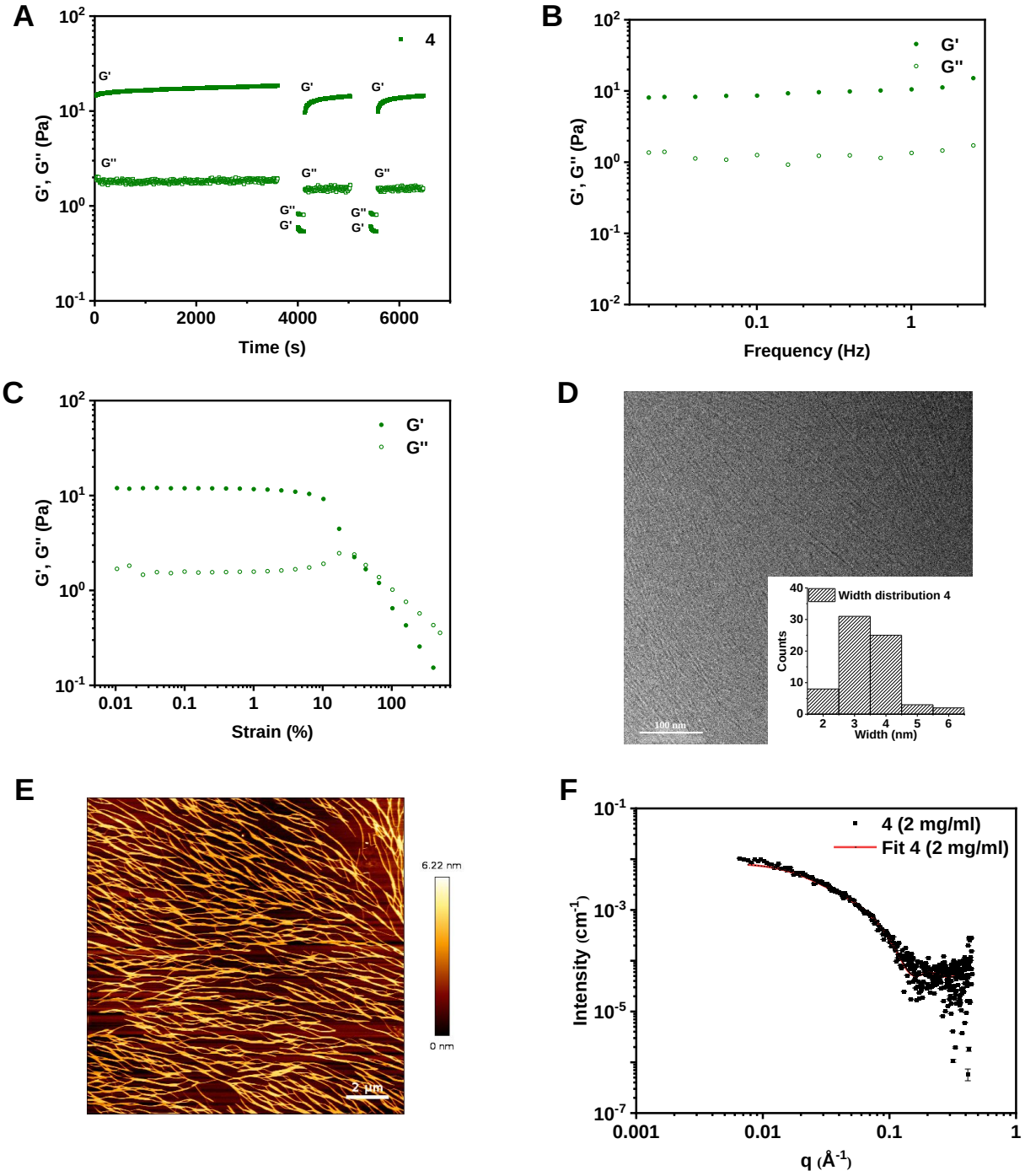

Figure 1. Oscillatory rheology measurements of hydrogels **4** (5 mM) in MilliQ water at RT: (A) Time sweep measurements (ƒ = 1 Hz, γ = 0.05%) and self-recovery process of hydrogel **4** (5 mM) in MilliQ water at RT. (B) Frequency sweep (γ = 0.05%). (C) Amplitude sweep (ƒ = 1 Hz). (D) Cryo-TEM images of **4** (0.5 mM) in Milli Q water. Insert Histograms of fiber width distribution for a sample size of N ≥ 50. Scale bar: *100 nm*. (E) AFM height image of **4** (0.25 mM) by spinning coating (2000 rpm, 2 min) and deposited on mica overnight after dissolution. (F) Small-angle X-ray scattering profiles of fibers **4** (2 mg/mL). Black dots represent experimental data; the red line represents fit with a form factor for flexible cylinders.

To understand the origin of the distinct mechanical properties of hydrogels **2**-**5**, we performed studies that permit insight into the morphological aspect of the assembled structures. Monomers **3**-**5** formed high-aspect ratio fibers on assembly reaching several micrometers in length by cryo-TEM imaging (Figure 1D, S12). Monomer **4** exhibited thicker supramolecular polymer fibers (4 nm) compared to **3** (3 nm) that contained an increased number of squaramide units, while **5** showed the

thickest fibers (5 nm) bearing the maximum number of squaramides and the carbamate group in place of the ether. Most likely, the weak mechanical properties measured by oscillatory rheology originate from the dense and entangled presentation of filamentous structures with the differences in moduli arising due to the differences in fibrillar diameter. Recorded AFM images of **3**, **4** and **5** further support the cryo-EM findings (Figure 1E, S13). Moreover, we found for monomer **2** (0.25 mM) sheet-like structures instead of fibers consistent with its lower solubility due to the introduction of an alkyl chain. Small-angle X-ray scattering (SAXS) further supported the differences in morphology of the supramolecular polymers **3**-**5** in water. The scattering profiles revealed the presence of elongated one-dimensional aggregates with high aspect ratios of solutions **3**-**5** (Figure 1F, S14). A form factor appropriate for flexible cylinders best described the obtained scattering profiles, yielding cross-sectional radii of 1.8 nm (**3**), 2.3 nm (**4**), and 2.4 nm (**5**) for the various monomers in line with earlier trends measured from cryoTEM images. These findings indicate that altering the hydrophilic and hydrogen bonding domains of the squaramide-based tripodal monomers can modulate the fiber properties.

We then probed the impact of supramolecular polymerization on monomers **1**-**5** at the molecular level by spectroscopic (UV, IR) methods. Monomer **5** displayed two distinct peaks at 270 and 323 nm in the UV spectra, corresponding to HOMO-LUMO and HOMO-LUMO+1 transitions of the squaramide moiety when polymerized in a head-to-tail hydrogen bonding arrangement (Figure 2A). Replacement of the carbamate moieties with ethers in the monomer **4** yielded a similar spectral profile to that of **5**, with red- and blue-shifted transitions observed at 271 nm and 321 nm but with reduced absorption intensity. Monomer **3** showed a distinct spectral profile with a sharp peak 324 nm and a plateau-like shoulder at 274 nm pointing out a distinct conformation of the squaramides within the monomer due to the alteration in their number and the hydrophobic and hydrophilic domains. The introduction of an alkyl chain in the third position of **2** to yield a more hydrophobic structure, led to a UV-Vis profile displaying two broad peaks at 257 nm and 318 nm with a lower intensity compared to **3**. Monomer **1** that lacked one squaramide moiety and one aliphatic spacer, exhibited a single band at 289 nm, suggesting a lack of polymerization due to the imbalance between the hydrophilic and hydrophobic domains and an insufficient number of hydrogen bonds. These results demonstrate that chemical modifications to the squaramide-based monomers at the periphery do not impact the orientation of the squaramides in the resulting supramolecular polymers, whereas those at the center result in distinct modes of monomer assembly. These UV-Vis studies can further benefit from computation to unravel the conformation of the monomers that lead to the observed polymer structures.

To gain further insight into the polymerization mechanism of the monomers **1**-**5**, we evaluated the effect of changes in concentration or addition of a co-solvent to the supramolecular polymers. Concentration-dependent UV-Vis absorption studies revealed that monomers **1**-**5** retained their peak shifts even with decreasing their concentration down to the sub-micromolar range (Figure 2B, S15). Because of the insensitivity of the formed supramolecular polymers to concentration changes, we used a co-solvent approach to depolymerize **1**-**5**. We titrated acetonitrile (MeCN) to supramolecular polymers of **3**-**5** in water. For all monomers, a H_2O-MeCN volume ratio of 6:4 yielded a single absorbance band at 293 nm consistent with depolymerization (Figure S16-S17). In solely MeCN, monomers **1**-**3** exhibited a single band in the same range as the other. Interestingly, monomers **4** and **5** in MeCN displayed two peaks at 290 and 321 nm and 294 and 323 nm, respectively, consistent with

head-to-tail squaramide assembly of the monomer similarly to water. The depolymerization of the monomers with a co-solvent opens the door to unravel the mechanism of the polymerization of the monomers and the influence of their distinct chemical structures on this process.

We then evaluated the changes in chemical structure on the hydrophobic domains presented by the aggregates on assembly by the Nile Red dye assay. Nile Red is a solvatochromic dye that shows a blue shift and an increase in the intensity of its fluorescence emission when embedded within a hydrophobic environment relative to water.[35,36] We observed a highly intense, blue-shifted emission band at 615 nm for **5**, whereas the emission maxima of **4** and **3** shifted to lesser extent at 623 nm and 621 nm, respectively, when we exchanged the carbamate moieties with ethers and further removed a squaramide unit (Figure 1C). The replacement of the third arm for an alkyl chain in monomer **2** resulted in a very low intensity emission band at 621 nm. Monomer **1** that lacked one squaramide moiety and one alkyl spacer showed a fluorescence emission profile as the dye in water in line with UV-Vis studies that suggest a lack of polymerization. These differences in emission maxima and intensity align with the changes in the hydrophobic and hydrophilic domains of the monomers and their distinctive modes of aggregation.[37-40]

We next examined the interactions between the monomers through Fourier Transform Infrared (FTIR) Spectroscopy on lyophilized samples and solutions. Lyophilized samples of **5** exhibited two distinct bands for the N-H stretch of the carbamate (3315 cm^{-1}) and squaramide units (3166 cm^{-1}), while the exchange of the carbamate for an ether bond in **2**-**4** displayed only one band for the squaramide unit (3169 - 3165 cm^{-1}) (Figure 2D, Table S1). Additionally, **5** displayed two extra C=O bands at 1719 cm^{-1} and 1689 cm^{-1} due to the carbamate moieities. The C-H stretches (both antisymmetric and symmetric) shifted slightly to a lower wavenumber because of the additional squaramide unit and carbamate groups in the monomer (Figure 2D, inset), and suggests a closer packing of the aliphatic chains within the supramolecular polymer.[41,42] We recorded a small independent ring breathing band at 1797 - 1799 cm^{-1} for monomers **2**-**5** consistent with the squaramide moiety. In the amide I region, all monomers possessed multiple C=O stretches originating from the carbamates and squaramides, that suggested the presence of several monomer packing modes in the polymerized state.

We performed infrared spectroscopy on monomers **3**-**5** in the solution state to probe the effect of adding a co-solvent to the polymers. The N-H stretch of the squaramide progressively moved to lower wavenumbers in **3**-**5** in D_2O (**3**: 3170 cm^{-1}, **4**: 3162 cm^{-1}, **5**: 3141 cm^{-1}), in line with stronger hydrogen bonds being formed by the squaramide moiety likely due to a more optimal packing of the monomers (Figure S18, Table S2). Alternatively, these peaks shifted to higher wavenumbers (**3**: 3174 cm^{-1}, **4**: 3166 cm^{-1}, **5**: 3155 cm^{-1}) when the solvent was changed to D_2O-CD_3CN (v/v-6:4) maintaining the same trend, pointing out that their depolymerization occurred. Furthermore, monomer **5** showed an extra band (1674 cm^{-1}) corresponding to the carbamate that shifted to a higher wavenumber (1692 cm^{-1}) on assembly in D_2O which aligns with our prior findings.[43] These results suggest that the squaramides play an important role in the assembly in the solid and solution state and solvents that compete with the association of the monomers trigger depolymerization affecting key interactions.

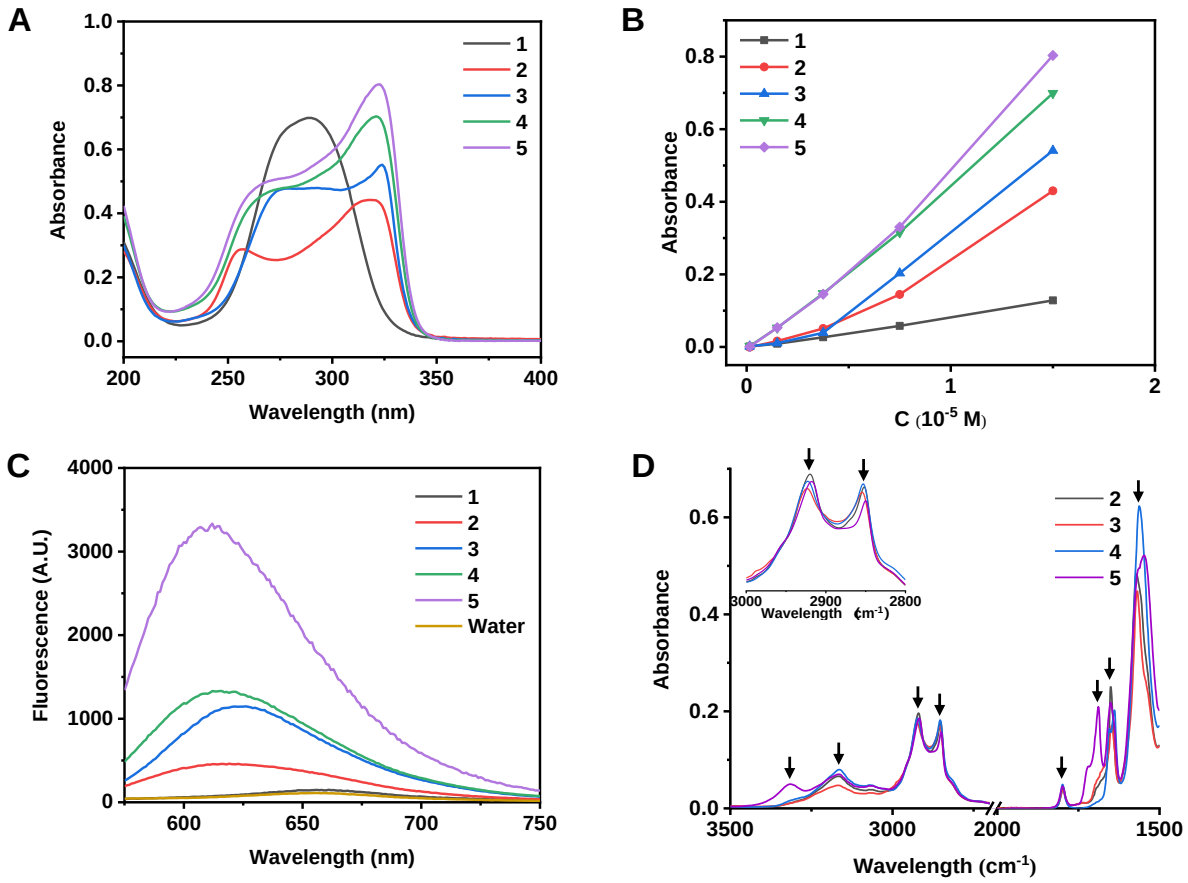

Figure 2. Spectroscopic studies of tripodal squaramide-based molecules: (A) UV-Vis spectra of **1**-**5** (15 µM) in water. (B) Concentration varied UV absorbance of **1**-**5** plotted at 322nm. (C) Fluorescence spectra (15 µM) of Nile Red dye embedded tripodal molecules **1**-**5**: ($c_{NileRed}$=0.005 mg/mL, λ_{exc} = 550 nm., λ_{em} = 560-750 nm), Nile red in water is used as a control. (D) FTIR spectra of **2**-**5** in the solid state (samples lyophilized from water (5 mM), arrows highlight peaks considered).

Squaramide-based hydrogels show thermal responsiveness and shape memory

Once insight into the various assembly modes of the monomers and their capacity to prepare gel phase materials was assessed we then evaluated their response to temperature. We first considered the effect of temperature on the supramolecular assemblies by UV-Vis thermal ramping experiments. Increasing the temperature of the various assembled monomer solutions in water resulted dehydration of oligoethylene glycol chains with a concomitant increase in turbidity of the samples due to their phase separation at a particular temperature, otherwise known as the lower critical solution temperature (LCST) (Figure S19). We recorded a LCST of ~52.5°C for **3** at 1 mM, whereas **4** with one additional squaramide unit showed a slightly higher value at ~60.5°C, and **5** demonstrated the highest LCST at ~69.0°C when the ether was replaced with the carbamate. These results illustrate that the LCST values of **3**, **4**, and **5** can be modulated according to the structural modification. Furthermore, when the decreasing the concentration to 0.2 mM, the LCST values increased to ~73.5°C for **5**, ~63.5°C for **4** and ~51.5°C for **3**, with **4** and **5** showing a higher sensitivity to concentration changes compared to **3** that showed a less significant variation, which is in line with similar studies for temperature-responsive polymers.[44,45] These results are likely due to the stronger interactions between the supramolecular polymer chain and water molecules due to the addition of squaramide unit and carbamate in **4** and **5**, which resulted in a more noticeable change in LCST compared with **3** has the minimal hydrogen bonds.[14,16,46] Strikingly, after heating **4** and **5** up to 90°C

in the cuvette and returning to room temperature the original state of the solution is retained (Figure S19B, insert). On the other hand, **3** appeared as a membrane-like precipitate after the heating process.

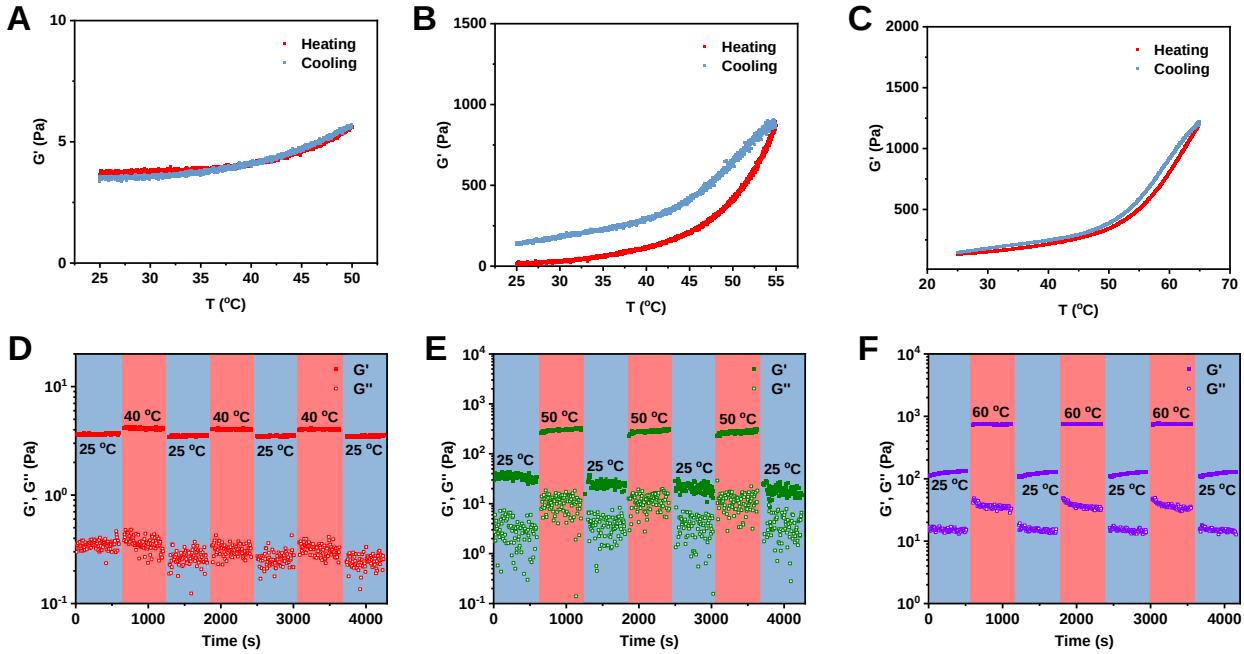

Figure 3. Self-healing properties of hydrogels (5 mM) (A) **3**, (B) **4**, (C) **5** in H_2O at different temperatures. Heating and cooling of hydrogels (5 mM) in various temperature ranges (D) **3** (25°C – 50°C), (E) **4** (25°C – 55°C), (F) **5** (25°C – 65°C) in H_2O.

We probed the mechanical response of the hydrogels **3**-**5** (5 mM) to temperature by conducting cyclic temperature sweep measurements on the rheometer. On the heating run, we observed an abrupt increase in the storage modulus (G') indicative of an LCST transition and thermal stiffening process for hydrogel **3** at 44.6°C, for gel **4** at 48.2°C and for hydrogel **5** at 71°C (Figure 3A-C), which showed the same trend as UV results with the increase in hydrogen bond number. Hydrogels **3** and **5** demonstrated nearly identical profiles during the heating and cooling process, indicating a high degree of recovery while hydrogel **4** showed hysteresis and did not fully recover after one temperature ramp. The cyclic temperature sweep measurements results demonstrated the reversible nature[47] of the thermal stiffening process in hydrogels **3**-**5**, as evidenced by the fully reversible storage modulus G' that could be reproduced over multiple cycles when kept at temperatures near the LCST of each monomer (Figure 3D-F). We then performed differential scanning calorimetry (DSC) measurements on the samples to further probe the phase-transition properties and thermal stability of hydrogels **3**-**5** (5 mM) (Figure S20). The recorded DSC profiles showed an endothermic shift at the same inflection point corresponding to the LCST transition in the rheological data. These findings are further consistent with the UV results and the structural variations of monomers **3**-**5**, indicating that the incorporation of squaramide units and an increase the number of hydrogen bonds result in an elevated LCST and a more significant release of energy during the LCST transition process.

To further explore the thermal behavior of hydrogel **3**-**5** above the LCST range, we subsequently heated hydrogels **3**-**5** in NMR tubes from RT to 90°C in an oil bath to monitor the macrophase separation process. During this process, hydrogels **3**-**5** transformed from transparent gels to opaque solids after reaching a certain temperature (**3**: ~41 °C, **4**: ~51 °C, **5**: ~68 °C) while maintaining a constant volume (Figure 4A). This onset of this transition in the sample aligned with the LCST transitions in the rheometer. Further heating caused the gels to shrink and become whiter. Reaching 130 °C resulted in

the white substance breaking apart due to boiling water inside the NMR tube. Upon cooling back to room temperature, the white substance regained transparency but could not recover to its original state.

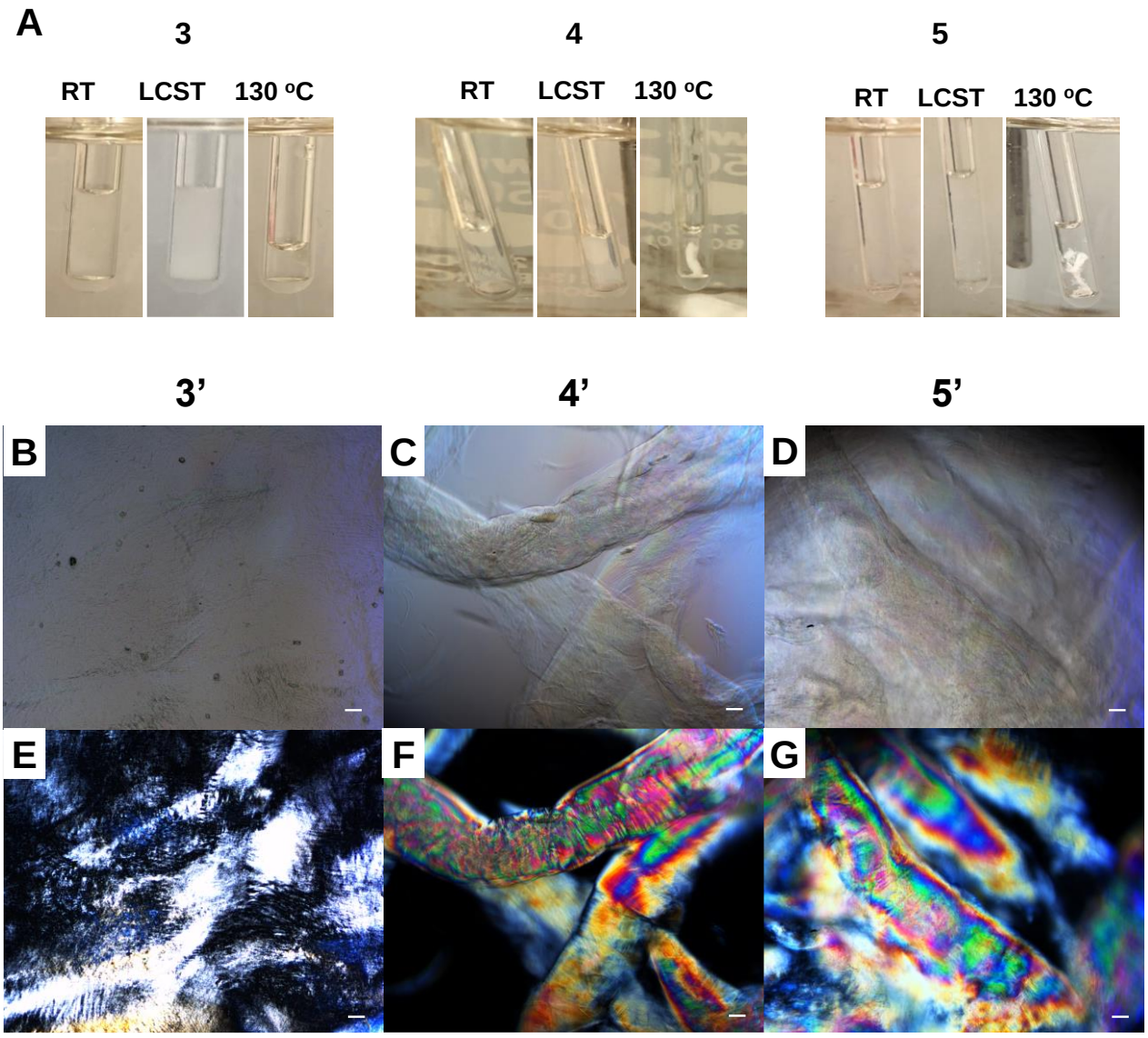

Figure 4. (A) Digital photos of hydrogel **3**-**5** (5 mM) during the heating process. Optical microscopy pictures and polarized optical microscopy (POM) of squaramide-based hydrogel prepared with H_2O after heating to 130°C and cooled back to RT: visible picture of **3'** (B), **4'** (C) and **5'** (D). POM micrographs of **3'** (E), **4'**(F), and **5'**(G). Scale bar: *100μm*.

Next, we employed polarizing microscopy (POM) to examine the optical properties of the annealed samples (**3'**, **4'**, **5'**) through exploring the birefringence of the substances. The POM images revealed that even after the heating process, the distinct shapes of **4'** and **5'** remained intact while **3'** was incomplete fragments, and we can observe the formation of colorful highly aligned substances with strong birefringence in **4'** and **5'**, while **3'** only displays slight birefringence (Figure 4B-G). Before heating, POM images of hydrogels **3**-**5** displayed a slight birefringence that is in line with cryo-TEM and AFM images showing alignment of some fibers after the self-assembly process (Figure S21). Scanning electron microscopy (SEM) images confirmed the presence of densely aligned fibers in **4** and **5**, while **3** exhibited a membrane-like morphology (Figure S22-S23). These structural differences among the hydrogels can be attributed to the alignment of fibers in hydrogels **4** and **5**, as observed in earlier cryo-

TEM images, that further consolidated during the heating process and lacked irreversibility upon cooling. However, monomer **3** lacked this behaviour, possibly due to the relatively weaker interactions between monomers with fewer hydrogen bonds that allowed disruption of its structure during the heating process.

We then examined the differences between the annealed samples at the molecular scale through X-ray diffraction (XRD) analysis. The low position peaks (**3'**: 4.36°, **4'**: 4.16°, **5'**: 3.83°) indicated an ordered structure of single fiber width while the peak around 21° signifies the presence of hydrophobic alkyl substituents (Figure S24). Additionally, the annealed samples (**3'**, **4'**, **5'**) showed reflections with a significantly stronger intensity compared to the non-annealed samples, indicating a higher orientation in the annealed fibers, and further explaining the difference in birefringence between samples.

In general, tripodal squaramide monomers **3**-**5** showed an organized fiber arrangement upon self-assembly in water, as observed through cryo-TEM, AFM and POM techniques. Upon heating, the water is removed from the oligo(ethylene glycols) between the supramolecular structures. It is hypothesized that **3**, with weaker and fewer molecular interactions between monomers, is more susceptible to a loss of stability when subjected to the removal of water molecules from the chains during the heating process. On the other hand, monomers **4** and **5**, with stronger molecular/fiber interactions due to the presence of the additional squaramide unit and carbamate, retain their stability, aggregating the fibers when exposed to a higher temperature above the LCST. We hypothesize that the greater orientation in the annealed fibers stems from the aggregation and fusion during the dehydration process.[48]

2.3 Conclusion

In this study, we performed systematic chemical modifications of the tripodal squaramide monomer reading out their effect on supramolecular polymerization and mechanical and thermal responsive properties of the hydrogels. The exchange of the carbamate for an ether linkage resulted in a reduction in hydrogel stiffness, whereas a reduction in the number of squaramide units and hydrophilic and hydrophobic properties still permitted the formation of gel phase materials that required a higher concentration of monomer and showed decreased stiffness. The observed effects on gelation likely result from the reduced degrees of polymerization of the squaramide monomers that affect supramolecular polymer entanglement. Additionally, thermo-responsive behaviors of hydrogels **3**-**5** varied according to their distinct hydrophilicity and hydrogen bonding units. After heating the hydrogels to 130°C and cooling them back to room temperature, we observed that the hydrogels **4** and **5** retained their original shapes but underwent shrinkage, eventually transforming into highly aligned materials. Cumulatively, these results point out the necessary structural features to guide gelation and tune thermal responsive properties of tripodal squaramide-based monomers in water, but also their hints at their tolerance to structural modifications for future works that involve their use as functional supramolecular biomaterials.

Reference

(1) Aida, T.; Meijer, E. W.; Stupp, S. I. Functional Supramolecular Polymers. *Science* **2012,** *335* (6070), 813.

(2) Yang, L.; Tan, X.; Wang, Z.; Zhang, X. Supramolecular Polymers: Historical Development, Preparation, Characterization, and Functions. *Chemical Reviews* **2015,** *115* (15), 7196.

(3) Dou, X.; Mehwish, N.; Zhao, C.; Liu, J.; Xing, C.; Feng, C. Supramolecular Hydrogels with Tunable Chirality for Promising Biomedical Applications. *Acc. Chem. Res.* **2020,** *53* (4), 852.

(4) Du, X.; Zhou, J.; Shi, J.; Xu, B. Supramolecular Hydrogelators and Hydrogels: From Soft Matter to Molecular Biomaterials. *Chem Rev* **2015,** *115* (24), 13165.

(5) Cheng, J.; Amin, D.; Latona, J.; Heber-Katz, E.; Messersmith, P. B. Supramolecular Polymer Hydrogels for Drug-Induced Tissue Regeneration. *ACS Nano* **2019,** *13* (5), 5493.

(6) Li, L.; Sun, R.; Zheng, R. Tunable morphology and functionality of multicomponent self-assembly: A review. *Materials & Design* **2021,** *197,* 109209.

(7) de Marco, A. L.; Bochicchio, D.; Gardin, A.; Doni, G.; Pavan, G. M. Controlling Exchange Pathways in Dynamic Supramolecular Polymers by Controlling Defects. *ACS Nano* **2021,** *15* (9), 14229.

(8) Bruckner, E. P.; Stupp, S. I. Designing supramolecular polymers with nucleation and growth processes. *Polym. Int.* **2022,** *71* (5), 590.

(9) Lotz, B.; Miyoshi, T.; Cheng, S. Z. 50th anniversary perspective: Polymer crystals and crystallization: Personal journeys in a challenging research field. *Macromolecules* **2017,** *50* (16), 5995.

(10) De Greef, T. F.; Smulders, M. M.; Wolffs, M.; Schenning, A. P.; Sijbesma, R. P.; Meijer, E. Supramolecular polymerization. *Chem. Rev.* **2009,** *109* (11), 5687.

(11) Sen, S. K.; Mukhopadhyay, R. D.; Choi, S.; Hwang, I.; Kim, K. Spatiotemporal segregation of chiral supramolecular polymers. *Chem* **2023,** *9* (3), 624.

(12) Leenders, C. M.; Albertazzi, L.; Mes, T.; Koenigs, M. M.; Palmans, A. R.; Meijer, E. W. Supramolecular polymerization in water harnessing both hydrophobic effects and hydrogen bond formation. *Chem Commun (Camb)* **2013,** *49* (19), 1963.

(13) Chassenieux, C.; Tsitsilianis, C. Recent trends in pH/thermo-responsive self-assembling hydrogels: from polyions to peptide-based polymeric gelators. *Soft Matter* **2016,** *12* (5), 1344.

(14) Zhang, Q.; Dong, S.; Zhang, M.; Huang, F. Supramolecular control over thermo-responsive systems with lower critical solution temperature behavior. *Aggregate* **2021,** *2* (1), 35.

(15) Yan, X.; Wang, F.; Zheng, B.; Huang, F. Stimuli-responsive supramolecular polymeric materials. *Chem. Soc. Rev.* **2012,** *41* (18), 6042.

(16) Xian, S.; Webber, M. J. Temperature-responsive supramolecular hydrogels. *J. Mater. Chem. B* **2020,** *8* (40), 9197.

(17) Lu, W.; Le, X.; Zhang, J.; Huang, Y.; Chen, T. Supramolecular shape memory hydrogels: a new bridge between stimuli-responsive polymers and supramolecular chemistry. *Chem. Soc. Rev.* **2017,** *46* (5), 1284.

(18) Lu, H.; Xing, Z.; Chen, M.; Yu, K.; Fu, Y. Q. Solvent-aided phase separation in hydrogel towards significantly enhanced mechanoresponsive strength. *Acta Mechanica Sinica* **2021,** *37*, 757.

(19) Chen, H.; Li, Y.; Tao, G.; Wang, L.; Zhou, S. Thermo- and water-induced shape memory poly(vinyl alcohol) supramolecular networks crosslinked by self-complementary quadruple hydrogen bonding. *Polymer Chemistry* **2016,** *7* (43), 6637.

(20) Zhang, G.; Chen, Y.; Deng, Y.; Ngai, T.; Wang, C. Dynamic Supramolecular Hydrogels: Regulating Hydrogel Properties through Self-Complementary Quadruple Hydrogen Bonds and Thermo-Switch. *ACS Macro Lett* **2017,** *6* (7), 641.

(21) Hao, L.; Yegin, C.; Talari, J. V.; Oh, J. K.; Zhang, M.; Sari, M. M.; Zhang, L.; Min, Y.; Akbulut, M.; Jiang, B. Thermo-responsive gels based on supramolecular assembly of an amidoamine and citric acid. *Soft Matter* **2018,** *14* (3), 432.

(22) Naya, M.; Kokado, K.; Landenberger, K. B.; Kanaoka, S.; Aoshima, S.; Sada, K. Supramolecularly designed thermoresponsive polymers in different polymer backbones. *Macromol. Chem. Phys.* **2020,** *221* (5), 1900455.
(23) Wang, F.; Gillissen, M. A.; Stals, P. J.; Palmans, A. R.; Meijer, E. W. Hydrogen bonding directed supramolecular polymerisation of oligo(phenylene-ethynylene)s: cooperative mechanism, core symmetry effect and chiral amplification. *Chemistry* **2012,** *18* (37), 11761.
(24) Hendricks, M. P.; Sato, K.; Palmer, L. C.; Stupp, S. I. Supramolecular Assembly of Peptide Amphiphiles. *Acc. Chem. Res.* **2017,** *50* (10), 2440.
(25) Jiang, Z. C.; Xiao, Y. Y.; Kang, Y.; Pan, M.; Li, B. J.; Zhang, S. Shape Memory Polymers Based on Supramolecular Interactions. *ACS Appl. Mater. Interfaces* **2017,** *9* (24), 20276.
(26) Merino, D. H.; Slark, A. T.; Colquhoun, H. M.; Hayes, W.; Hamley, I. W. Thermo-responsive microphase separated supramolecular polyurethanes. *Polymer Chemistry* **2010,** *1* (8), 1263.
(27) Zhang, G.; Chen, Y.; Deng, Y.; Ngai, T.; Wang, C. Dynamic supramolecular hydrogels: regulating hydrogel properties through self-complementary quadruple hydrogen bonds and thermo-switch. *ACS Macro Letters* **2017,** *6* (7), 641.
(28) Lugger, S. J. D.; Houben, S. J. A.; Foelen, Y.; Debije, M. G.; Schenning, A.; Mulder, D. J. Hydrogen-Bonded Supramolecular Liquid Crystal Polymers: Smart Materials with Stimuli-Responsive, Self-Healing, and Recyclable Properties. *Chem Rev* **2022,** *122* (5), 4946.
(29) Guo, M.; Pitet, L. M.; Wyss, H. M.; Vos, M.; Dankers, P. Y.; Meijer, E. W. Tough stimuli-responsive supramolecular hydrogels with hydrogen-bonding network junctions. *J. Am. Chem. Soc.* **2014,** *136* (19), 6969.
(30) Feng, Z.; Zuo, H.; Gao, W.; Ning, N.; Tian, M.; Zhang, L. A Robust, Self-Healable, and Shape Memory Supramolecular Hydrogel by Multiple Hydrogen Bonding Interactions. *Macromol. Rapid Commun.* **2018,** *39* (20), e1800138.
(31) Leenders, C. M.; Baker, M. B.; Pijpers, I. A.; Lafleur, R. P.; Albertazzi, L.; Palmans, A. R.; Meijer, E. W. Supramolecular polymerisation in water; elucidating the role of hydrophobic and hydrogen-bond interactions. *Soft Matter* **2016,** *12* (11), 2887.
(32) Taylor, M. J.; Tomlins, P.; Sahota, T. S. Thermoresponsive gels. *Gels* **2017,** *3* (1), 4.
(33) Xin, F.; Lyu, Q. A Review on Thermal Properties of Hydrogels for Electronic Devices Applications. *Gels* **2022,** *9* (1), 7.
(34) Tong, C.; Liu, T.; Saez Talens, V.; Noteborn, W. E. M.; Sharp, T. H.; Hendrix, M.; Voets, I. K.; Mummery, C. L.; Orlova, V. V.; Kieltyka, R. E. Squaramide-Based Supramolecular Materials for Three-Dimensional Cell Culture of Human Induced Pluripotent Stem Cells and Their Derivatives. *Biomacromolecules* **2018,** *19* (4), 1091.
(35) Haidekker, M. A.; Nipper, M.; Mustafic, A.; Lichlyter, D.; Dakanali, M.; Theodorakis, E. A. Dyes with segmental mobility: molecular rotors. *Advanced fluorescence reporters in chemistry and biology I: fundamentals and molecular design* **2010**, 267.
(36) Martinez, V.; Henary, M. Nile red and nile blue: applications and syntheses of structural analogues. *Chemistry–A European Journal* **2016,** *22* (39), 13764.
(37) Mako, T. L.; Racicot, J. M.; Levine, M. Supramolecular luminescent sensors. *Chem. Rev.* **2018,** *119* (1), 322.
(38) Wang, Y.; Wu, H.; Hu, W.; Stoddart, J. F. Color-Tunable Supramolecular Luminescent Materials. *Adv. Mater.* **2022,** *34* (22), 2105405.
(39) Rajdev, P.; Ghosh, S. Fluorescence resonance energy transfer (FRET): a powerful tool for probing amphiphilic polymer aggregates and supramolecular polymers. *The Journal of Physical Chemistry B* **2018,** *123* (2), 327.
(40) Hu, Y. X.; Li, W. J.; Jia, P. P.; Wang, X. Q.; Xu, L.; Yang, H. B. Supramolecular Artificial Light-Harvesting Systems with Aggregation-Induced Emission. *Advanced Optical Materials* **2020,** *8* (14), 2000265.
(41) Yang, M.; Zhang, Z.; Yuan, F.; Wang, W.; Hess, S.; Lienkamp, K.; Lieberwirth, I.; Wegner, G. Self-assembled structures in organogels of amphiphilic diblock codendrimers. *Chemistry–A European Journal* **2008,** *14* (11), 3330.

(42) Nebot, V. J.; Armengol, J.; Smets, J.; Prieto, S. F.; Escuder, B.; Miravet, J. F. Molecular hydrogels from bolaform amino acid derivatives: A structure–properties study based on the thermodynamics of gel solubilization. *Chemistry–A European Journal* **2012,** *18* (13), 4063.
(43) Saez Talens, V.; Davis, J.; Wu, C. H.; Wen, Z.; Lauria, F.; Gupta, K.; Rudge, R.; Boraghi, M.; Hagemeijer, A.; Trinh, T. T.et al. Thiosquaramide-Based Supramolecular Polymers: Aromaticity Gain in a Switched Mode of Self-Assembly. *J. Am. Chem. Soc.* **2020,** *142* (47), 19907.
(44) Chen, F.; Lu, G.; Yuan, H.; Li, R.; Nie, J.; Zhao, Y.; Shu, X.; Zhu, X. Mechanism and regulation of LCST behavior in poly (hydroxypropyl acrylate)-based temperature-sensitive hydrogels. *Journal of Materials Chemistry A* **2022,** *10* (35), 18235.
(45) Kojima, H. Studies on the phase transition of hydrogels and aqueous solutions of thermosensitive polymers. *Polym. J.* **2018,** *50* (6), 411.
(46) Liu, H.; Prachyathipsakul, T.; Koyasseril-Yehiya, T. M.; Le, S. P.; Thayumanavan, S. Molecular bases for temperature sensitivity in supramolecular assemblies and their applications as thermoresponsive soft materials. *Materials horizons* **2022,** *9* (1), 164.
(47) Wei, Y.; Zheng, L.; Xie, X.; Yang, X.; Liao, J. Recent advances in stimuli responsive hydrogels for oral disease treatment. *Materials & Design* **2024**, 112817.
(48) Zhang, S.; Greenfield, M. A.; Mata, A.; Palmer, L. C.; Bitton, R.; Mantei, J. R.; Aparicio, C.; de la Cruz, M. O.; Stupp, S. I. A self-assembly pathway to aligned monodomain gels. *Nat. Mater.* **2010,** *9* (7), 594.

Supporting Information

S2.1 Materials and methods

Materials

O-methyl-undecaethylene glycol was obtained from polypure and Broadpharm. Compounds **5** and **10** were synthesized as previously reported.[1] Potassium phthalimide, hydrazine monohydrate, sodium and all other commercially available chemicals were purchased from Sigma Aldrich and used without further purification. Lacey carbon 200 mesh grids were purchased from Electron Microscopy Sciences. Deuterated solvents for NMR experiments were obtained from Euriso-top. Milli-Q water (H_2O) was employed for all the experiments. All the compounds were stored at -20^oC until further usage.

Methods

^{1}H-NMR and ^{13}C-NMR spectra were recorded on a Bruker DMX-300. All the final compounds were purified by high performance liquid chromatography (HPLC) on a Shimadzu system equipped with two LC-20AR pumps, an SPD-20A UV-Vis detector and Phenomenex Kinetex EVO C18 column. The mobile phase used consisted of CH_3CN and H_2O with 0.1% trifluoroacetic acid and the purity of the compounds was assessed by LC-MS. LC-MS analysis was performed on a Finnigan Surveyor HPLC system equipped (UV detection from 200-600 nm) with a Gemini C18 50 x 4.60 mm reverse phase column coupled to Finnigan LCQ Advantage Max mass spectrometer with ESI. For the mobile phase, a gradient of 10-90% of CH_3CN/H_2O with 0.1% trifluoroacetic acid over 13.5 minutes was used. High resolution mass spectra (HR-MS) were collected on Q-Exactive HF Orbitrap mass spectrometer from Thermo Scientific that equipped with an electrospray ion source (ESI). The spectra were collected by direct injection of a 2 µL aliquot of the sample solution (1 µM) into Ultimate 3000 nano UPLC (Dionex) with an external calibration using source voltage of 3.5kV, capillary temperature 275˚C, resolution = 240000 at *m/z* = 400, mass range *m/z* = 160-2000 or until a maximum of 6000. Eluents used: CH_3CN:H_2O (1:1 v/v) supplemented with 0.1% formic acid. UV absorption spectra were acquired at room temperature (RT) on a Cary 300 UV-Vis spectrophotometer from 400 to 800 nm using a quartz cuvette with a path length of 1 cm equipped with a temperature control system. Fluorescence spectra were recorded on a TECAN Infinite M1000 PRO fluorescence plate reader. FTIR spectra in the solid state were recorded on a PerkinElmer Spectrum Two UATR FT-IR spectrometer with a resolution of 4 cm^{-1}. Fourier transform infrared spectroscopy (FTIR) spectra in the solution state were obtained on a Bruker Tensor 27 IR spectrometer with a resolution of 1 cm^{-1} averaged over 128 scans at RT. The supramolecular fiber morphologies were imaged on a Talos L120C cryogenic electron microscope (cryo-EM) operating at 120 kV, samples were plunge frozen on a Vitrobot Mark IV, both from Thermo Fisher Scientific. Atomic force (AFM) micrographs were recorded on a JPK Nanowizard Ultra AFM using silicon cantilever tips with a 70 kHz resonance frequency and 2 N/m force constant. The surface morphology and annealed hydrogels were imaged by scanning electron microscope (SEM). The critical gelation concentration (CGC) was determined from the gel inversion method. Oscillatory rheology experiments were performed on a Discovery Hybrid Rheometer purchased from TA Instruments with a temperature controller using a parallel plate geometry (40 mm diameter) with a fixed gap (0.6 mm). Differential scanning calorimetry (DSC) test were measured in a nano DSC purchased from TA Instruments to determine the endothermic and exothermic curves. X-Ray diffraction (XRD) analysis were performed using a Bruker D8 Advance diffractometer with a Bragg-Brentano geometry and

equipped with a Cu-Kα X-ray source that has a wavelength of 1.54 Å in 2θ ranging from 2.5 to 30˚. Polarized optical images (POM) were probed on an Olympus BH-2 microscope. Small angle X-ray scattering measurements (SAXS) were carried out on a SAXSLAB GANESHA 300 XL SAXS system equipped with a GeniX 3D Cu ultralow divergence microfocus sealed tube source producing X-rays with a wavelength λ = 1.54 Å at a flux of $1x10^8$ ph/s, and a Pilatus 300K silicon pixel detector with 487 x 619 pixels of 172 µm x172 µm in size, which is placed at two sample-to-detector distances of 713 and 1513 mm respectively to access a q-range of $0.009 \leq q \leq 0.456$ $Å^{-1}$, where $q = 4\pi/\lambda(\sin \theta/2)$. The calibration of the beam center and q-range was achieved by using silver behenate. Samples were prepared on a Branson 2510 Ultrasonic Cleaner ice bath for ~20 minutes.

Synthetic Procedures

Synthetic routes of monomers 1-4

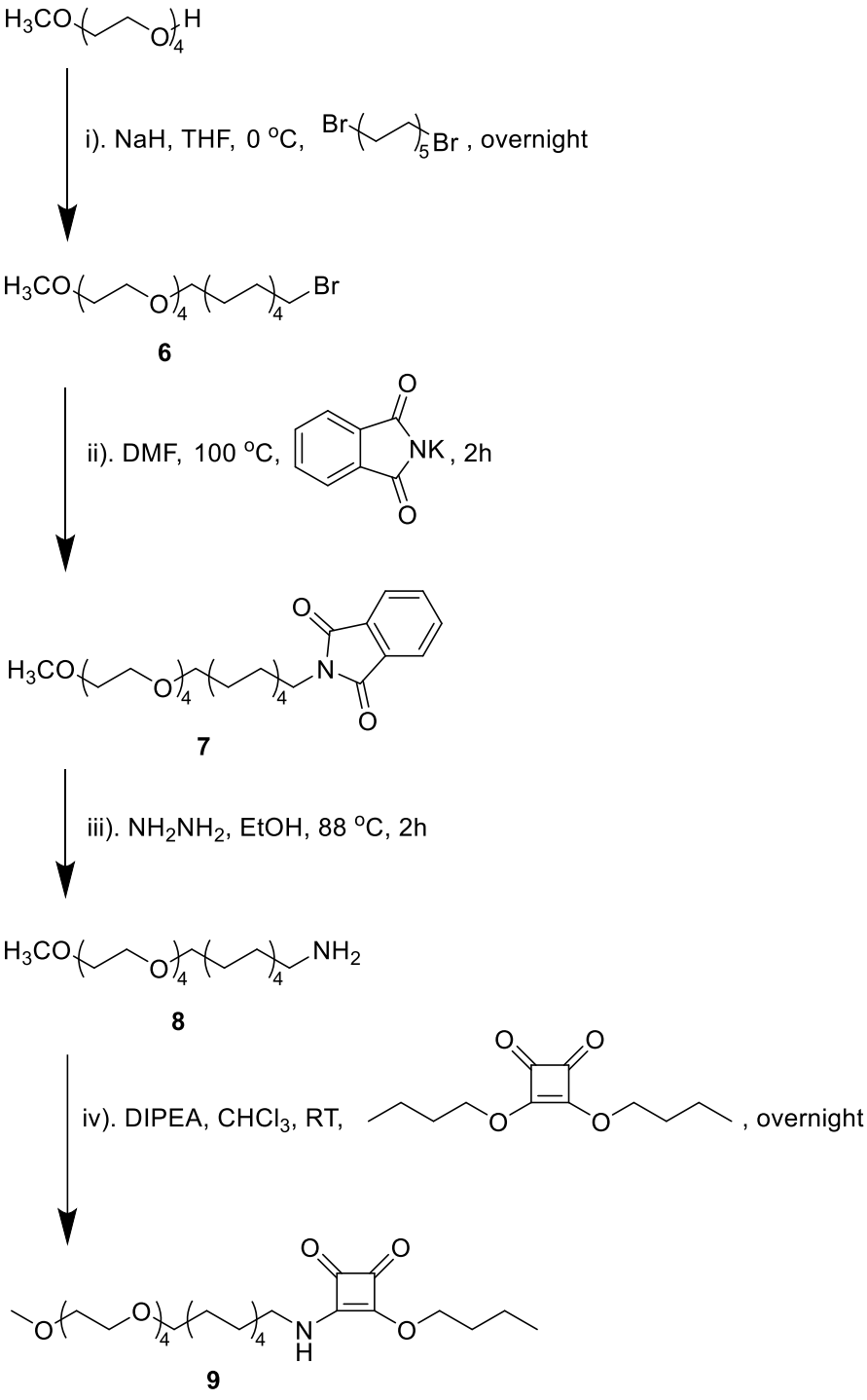

Figure S1. Synthetic route of monomer **9**.

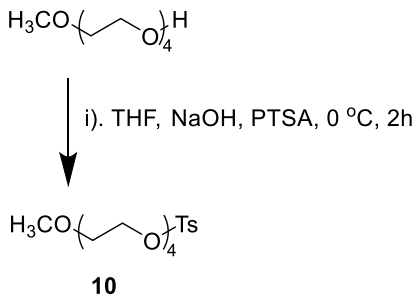

Figure S2. Synthetic route of monomer **10**.

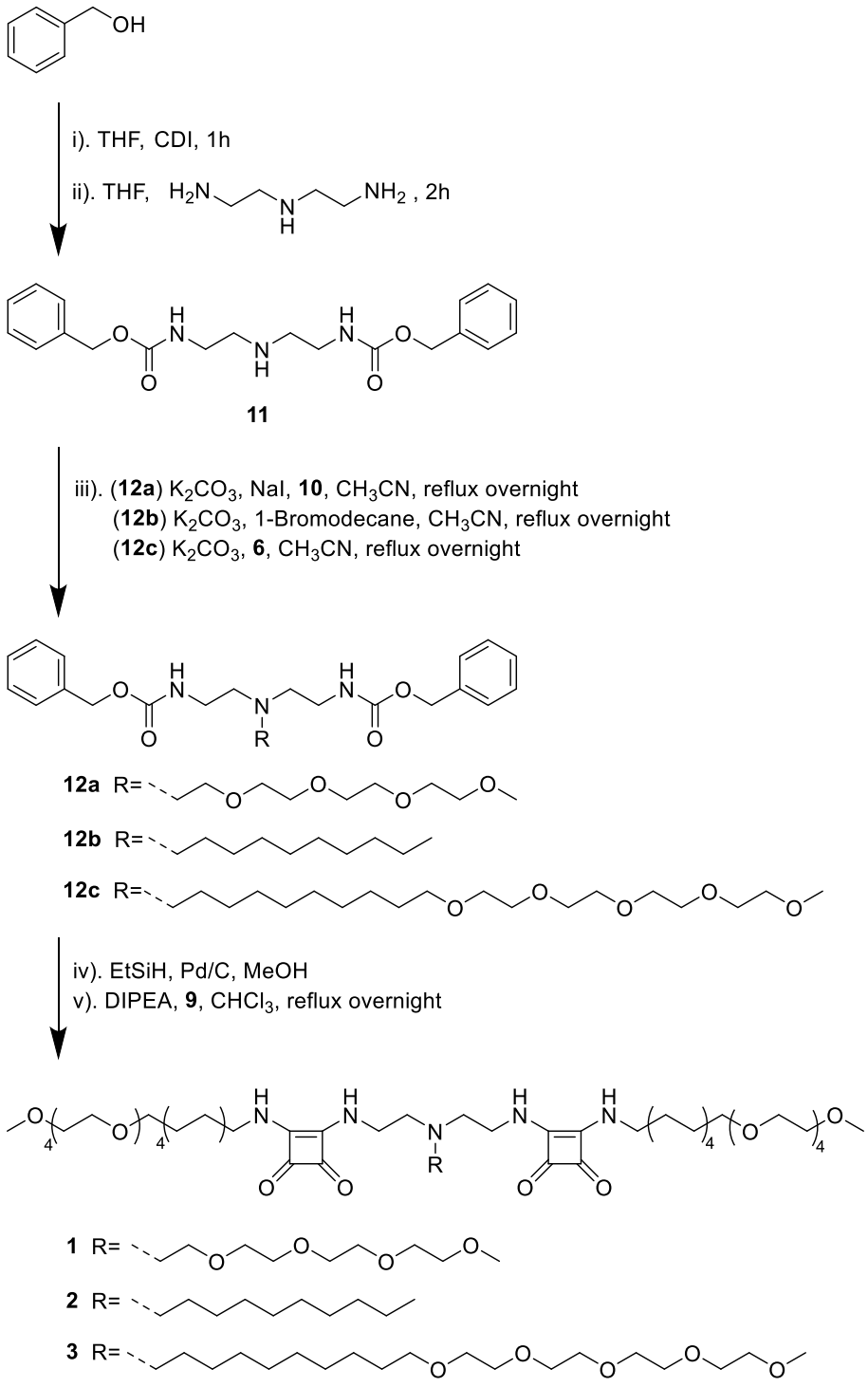

Figure S3. Synthetic route of monomers **1**-**3**.

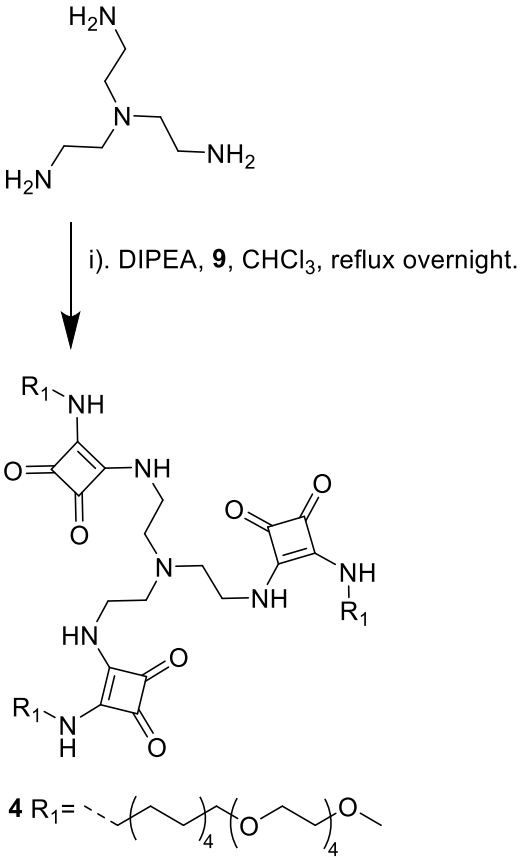

Figure S4. Synthetic route of monomer **4**.

Structure of monomer 5

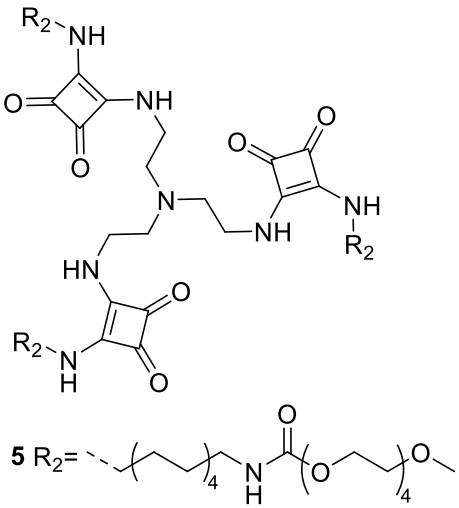

Figure S5. Structure of tripodal squaramide-based monomer **5**.

Synthesis of 6

A dispersion of sodium hydride in mineral oil (60%) (0.77 g, 19.23 mmol) was added in small portions to a stirring solution of tetraethylene glycol monomethyl ether (4.0 g, 19.23 mmol) in dry THF (40 mL) at 0°C, resulting in a foaming grey solution. The ice bath was removed once the foam ceased. Subsequently, 1,10-dibromodecane (11.56 g, 38.46 mmol) was added and the reaction mixture was stirred overnight at RT. H_2O was added to the reaction mixture (20 mL) and extracted with Et_2O (3 x 40 mL). The combined organic layers were collected, dried with Na_2SO_4, filtered, and concentrated in vacuum. The crude was purified by silica column chromatography (EtOAc/Pet ether: 10/90 - 30/70) to obtain the product as a colorless oil.

Yield = 5.27 g, 64.3 %. ^{1}H NMR (300 MHz, $CDCl_3$): δ (ppm) = 3.58-3.46 (m, 16H), 3.39-3.30 (m, 5H), 1.79-1.72 (t, 2H), 1.52-1.47 (t, 2H), 1.35-1.22 (d, 14H). ^{13}C NMR (75 MHz, $CDCl_3$): δ (ppm) = 71.87, 71.38, 70.53, 70.45, 70.01, 58.94, 33.87, 33.74, 32.72, 29.56, 29.38, 29.35, 29.29, 28.99, 28.83, 28.66, 28.08, 26.00. HRMS (ESI) *m/z*: $[M+H]^+$ calcd. for $C_{19}H_{40}O_5Br$: 427.20536; found: 427.20391. LC-MS: *t* = 8.95 min, *m/z*: 448.38 $[M+Na]^+$.

Synthesis of 7

6 (4.04 g, 9.45 mmol) and potassium phthalimide (2.45 g, 13.23 mmol) were dissolved in dry DMF (30 mL) and the mixture was heated to reflux for 2 hours. After the removal of the solvent by rotary evaporation, the residue was redissolved in CH_2Cl_2 (50 mL), washed with 1M HCl (2 x 30 mL), dried with Na_2SO_4, filtered, and concentrated in vacuum. The crude was purified by silica column chromatography (EtOAc/Pet ether: 10/90 – 30/70) to obtain the product as a colorless oil.

Yield = 4.18 g, 85.7 %. ^{1}H NMR (300 MHz, $CDCl_3$): δ (ppm) = 7.84-7.68 (d, 4H), 3.68-3.56 (m, 18H), 3.56-3.42 (m, 2H), 3.36 (s, 3H), 1.67-1.50 (m, 4H), 1.24 (m, 14H). ^{13}C NMR (75 MHz, $CDCl_3$): δ (ppm) = 168.43, 134.27, 132.16, 123.18, 71.92, 71.50, 70.60, 70.58, 70.55, 70.50, 70.03, 58.76, 38.04, 29.60, 29.47, 29.40, 29.14, 28.57, 26.83, 26.03. HRMS (ESI) *m/z*: $[M+H]^+$ calcd. for $C_{27}H_{44}NO_7$, 494.31123; found, 494.31392. LC-MS: t =8.51 min, *m/z*: 515.34 $[M+H]^+$.

Synthesis of 8

Hydrazine monohydrate (3.81 mL, 78.34 mmol) was added to a stirring solution of **7** (2.69 g, 5.45 mmol) in ethanol (50 mL) and the mixture was refluxed overnight. The solvent was removed by rotary evaporation and the mixture was dissolved in $CHCl_3$ (100 mL), extracted with 1M NaOH (3 x 100 mL) and the organic layers were collected and dried with Na_2SO_4, filtered, and concentrated in vacuum. The product was obtained as a colorless oil and used for the next step without any further purification.

Yield = 1.64 g, 82.9 %. ^{1}H NMR (300 MHz, $CDCl_3$): δ (ppm) = 3.53-3.40 (m, 16H), 3.34-3.29 (t, 2H), 3.25 (s, 3H), 2.57-2.53 (t, 2H), 1.46-1.15 (m, 18H). ^{13}C NMR (75 MHz, $CDCl_3$): δ (ppm) = 71.83, 71.39, 70.51, 70.48, 70.46, 70.40, 69.96, 58.81, 41.99, 33.42, 29.53, 29.45, 29.43, 29.36, 26.78, 25.98. HRMS (ESI) *m/z*: $[M+H]^+$ calcd. for $C_{19}H_{42}NO_5$, 364.30575; found, 364.30517. LC-MS: t =4.56 min, *m/z*: 363.52 $[M]^+$.

Synthesis of 9

8 (1.18 g, 3.26 mmol), 3,4-dibutoxy-3-cyclobutene-1,2-dione (0.87 mL, 3.91 mmol), and DIPEA (0.85 mL, 4.89 mmol) were dissolved in $CHCl_3$ (50 mL) and were stirred at RT for 2 h. The crude washed with H_2O (2 x 50 mL), dried with Na_2SO_4, filtered, and concentrated in vacuum. The crude was purified by silica column chromatography (EtOAc/Pet ether: 10/90 – 30/70) to obtain the final product as a light yellow oil.

Yield = 1.07 g, 63.9 %. ^{1}H NMR (300 MHz, $CDCl_3$): δ (ppm) = 7.26-7.24 (m, 1H), 4.71-4.62 (t, 2H), 3.60-3.47 (m, 16H), 3.41-3.32 (t, 6H), 1.78-1.68 (m, 2H), 1.58-1.22 (m, 18H), 0.94-0.89 (t, 3H). ^{13}C NMR (75 MHz, $CDCl_3$): δ (ppm) = 189.7, 172.37, 137.88, 73.30, 71.85, 71.41, 70.54, 70.51, 70.49, 70.42, 58.98, 44.84, 31.96, 30.61, 29.55, 29.42, 29.36, 29.07, 26.33, 26.00, 18.59, 13.74. HRMS (ESI) *m/z*: $[M+H]^+$ calcd. for $C_{27}H_{50}NO_8$, 516.35309; found, 516.35249. LC-MS: t =7.73 min, *m/z*: 515.62 $[M]^+$.

Synthesis of 10

10 was prepared according to a previously published protocol.[1] A solution of NaOH (0.88 g in 3 mL H_2O) was added to a stirring solution of tetraethylene glycol monomethyl ether (2.50g, 12.00 mmol) in THF (3.5 mL) at 0°C. After 15 minutes, 4-toluenesulfonyl chloride (2.25 g in 5 mL THF) was added dropwise and the reaction was allowed to stir at RT for 30 minutes. The solvent was removed by rotary evaporation and the reaction mixture was dissolved in H_2O (25 mL) and extracted with Et_2O (3 x 25 mL). The organic layers were collected and dried with Na_2SO_4, filtered, and concentrated in vacuum. The product was obtained as a colorless oil and used for the next step without any further purification.

Yield = 3.08 g, 70.7%. ^{1}H NMR (300 MHz, $CDCl_3$): δ (ppm) = 7.59-7.57 (d, 2H), 7.17-7.15 (d, 2H), 3.96-3.93 (t, 2H), 3.48-3.31 (m, 14H), 3.15 (s, 3H), 2.24 (s, 3H). 13C NMR (75 MHz, $CDCl_3$): δ (ppm) = 144.67, 132.84, 129.73, 127.71, 71.69, 70.40, 70.33, 70.27, 70.23, 69.29, 68.38, 58.68, 21.37. HRMS (ESI) *m/z*: $[M+H]^+$ calcd. for $C_{16}H_{27}O_7S$, 363.14720; found: 363.14720. LC-MS: t =7.82 min, *m/z*: 362.14 $[M]^+$.

Synthesis of 11

Benzyl alcohol (1.67 g, 15.42 mmol) and carbonyldiimidazole (3.0 g, 12.85 mmol) were dissolved in THF (50 mL) and stirred at RT for 30 minutes. Diethylenetriamine (0.6 mL, 5.77 mmol) was slowly added and stirred overnight at RT. The reaction mixture was extracted using EtOAc (3 x 50 mL) and the combined organic layers were collected and dried with Na_2SO_4, filtered, and concentrated in vacuum. The crude was purified by silica column chromatography (EtOAc/Pet ether: 50/50 – 100/0) to obtain the final product as a white solid.

Yield = 1.64 g, 76.5%. ^{1}H NMR (300 MHz, $CDCl_3$): δ (ppm) = 7.33 (s, 10H), 5.33 (s, 2H), 5.10 (s, 4H), 3.28-3.26 (t, 4H), 2.75-2.73 (t, 4H), 1.33 (s, 1H). ^{13}C NMR (75 MHz, $CDCl_3$): δ (ppm) = 156.69, 136.56, 128.50, 128.09, 66.71, 48.62, 40.74. HRMS (ESI) *m/z*: $[M+H]^+$ calcd. for $C_{20}H_{26}N_3O_4$, 372.19178; found, 372.19154. LC-MS: t = 5.11 min, *m/z*: 371.43 $[M]^+$.

Synthesis of 12a

10 (0.42 g, 1.15 mmol), **11** (0.23 g, 0.62 mmol), K_2CO_3 (0.12 g, 0.88 mmol), and sodium iodide (0.096 g, 0.64 mmol) were dissolved in dry CH_3CN (15 mL) and refluxed for 36 hours. The solvent was removed by rotary evaporation and the reaction mixture was redissolved in CH_2Cl_2 (25 mL), extracted with 1M NaOH (3 x 25 mL). The organic layers were collected and dried with Na_2SO_4, filtered, and concentrated in vacuum. The crude was purified by silica column chromatography (EtOAc/PE: 20/80 – 0/100) to obtain the final product as a colorless oil.

Yield = 0.31 g, 88.5%. ^{1}H NMR (300 MHz, $CDCl_3$): δ (ppm) = 7.29 (s, 10H), 5.91 (t, 2H), 5.05 (s, 4H), 3.64-3.40 (s, 14H), 3.33 (s, 3H), 3.22-3.16 (q, 4H), 2.61 (t, 6H). ^{13}C NMR (75 MHz, $CDCl_3$): δ (ppm) = 156.81, 136.87, 128.48, 128.05, 127.90, 71.77, 70.49, 70.46, 70.35, 70.32, 70.16, 69.99, 66.33, 58.71, 54.24, 53.20, 39.04. HRMS (ESI) *m/z*: $[M+H]^+$ calcd. for $C_{29}H_{44}N_3O_8$, 562.31229; found, 562.31153. LC-MS: t =5.46 min, 561.31 *m/z*: $[M]^+$.

Synthesis of 1

Triethylsilane (4.5 mL, 26.50 mmol) was added dropwise to a stirring solution of **12a** (243.50 mg, 0.43 mmol) and palladium on carbon (80 mg, 0.72 mmol) in dry CH_3OH (10 mL) under a N_2 atmosphere. The reaction was kept stirring overnight and then was filtered over celite, concentrated, and dissolved in $CHCl_3$ (50 mL). Subsequently, **1** (492.16 mg, 0.95 mmol) and DIPEA (0.33 mL, 1.90 mmol) were added to the reaction mixture and kept at reflux overnight. The solvent was removed by rotary evaporation and the residue was redissolved in CH_2Cl_2 (20 mL), washed with 1M HCl (3 x 10 mL). The combined organic fractions were collected and dried with $MgSO_4$, filtered, and concentrated in vacuum. The crude was purified by silica column chromatography (EtOAc: 100% – CH_3OH/ CH_2Cl_2: 10/90) to obtain the final product as a yellow oil. The compound was further purified by HPLC and lyophilized to obtain a yellow sticky solid.

Yield = 0.122 g, 40.6 %.^{1}H NMR (300 MHz, $CDCl_3$): δ (ppm) = 3.59 (m, 50H), 3.42 (t, 8H), 3.35 (s, 6H), 3.31 (s, 3H), 2.68 (m, 6H), 1.58 (m, 12H), 1.24 (s, 20H). ^{13}C NMR (75 MHz, $CDCl_3$): δ (ppm) = 183.25, 181.50, 168.98, 168.81, 72.26, 71.82, 71.67, 71.49, 70.87, 70.53, 70.49, 70.44, 70.36, 69.92, 58.98, 57.15, 53.89, 44.61, 43.52, 31.14, 29.55, 29.51, 29.44, 29.25, 26.50, 26.03. HRMS (ESI) *m/z*: $[M+H]^+$ calcd. for $C_{59}H_{110}N_5O_{18}$, 1176.78404; found, 1176.78445. LC-MS: t = 6.19 min, *m/z*: 1175.43 $[M]^+$.

Synthesis of 12b

11 (0.21 g, 0.58 mmol), 1-bromodecane (0.14 mL, 0.67 mmol) and K_2CO_3 (0.37 g, 2.69 mmol) were dissolved in dry CH_3CN (30 mL) and was relfluxed overnight. The solvent was removed by rotary evaporation and the reaction mixture was dissolved in CH_2Cl_2 (25 mL) and extracted with 1M NaOH (3 x 25 mL). The organic layers were collected and dried with Na_2SO_4, filtered, and concentrated in vacuum. The crude was purified by silica column chromatography (EtOAc/Pet ether: 10/90 – 50/50) to obtain the final product as a white solid.

Yield = 0.24 g, 81.1 %. ^{1}H NMR (300 MHz, $CDCl_3$): δ (ppm) = 7.32 (s, 10H), 5.08 (s, 4H), 3.45-3.19 (t, 2H), 3.30-3.19 (m, 4H), 2.62-2.43 (m, 4H), 1.39-1.26 (d, 16H), 0.93-0.88 (t, 3H). ^{13}C NMR (75 MHz, $CDCl_3$): δ (ppm) = 156.68, 136.72, 128.44, 128.01, 127.98, 66.56, 54.03, 53.51, 38.86, 34.01, 31.93, 31.90, 29.71, 29.62, 29.53, 29.36, 29.30, 27.39, 26.89, 22.71, 14.16. HRMS (ESI) *m/z*: $[M+H]^+$ calcd. for $C_{30}H_{46}N_3O_4$, 512.34381; found, 512.34726. LC-MS: t = 7.68 min, 511.70 *m/z*: $[M]^+$.

Synthesis of 2

Triethylsilane (4.0 mL, 25.21 mmol) was added dropwise to a stirring mixture solution of **12b** (215.2 mg, 420.6 mmol) and palladium on carbon (80 mg, 0.72 mmol) in dry CH_3OH (10 mL) under a N_2 atmosphere and kept at RT for overnight. The solution was filtered over celite, concentrated and dissolved in $CHCl_3$ (50 mL). **1** (477.1 mg, 0.93 mmol) and DIPEA (0.32 mL, 1.85 mmol) were added to the reaction mixture and heated to reflux overnight. The solvent was removed by rotary evaporation and the residue was redissolved in CH_2Cl_2 (20 mL) and washed with 1M HCl (3 x 10 mL). The combined organic fractions were collected and dried with $MgSO_4$, filtered, and concentrated in vacuum. The crude was purified by silica column chromatography (EtOAc: 100% – CH_3OH/CH_2Cl_2: 10/90) to obtain the final product as a yellow oil. The compound was further purified by HPLC and lyophilized to obtain a white solid.

Yield = 0.17 g, 47.1%. ^{1}H NMR (300 MHz, $CDCl_3$): δ (ppm) = 8.28 (s, 4H), 3.65-3.40 (m, 44H), 3.37 (s, 6H), 2.87-2.73 (t, 6H), 1.64-1.53 (m, 12H), 1.30-1.23 (m, 36H), 0.88-0.84 (m, 3H). ^{13}C NMR (75 MHz, $CDCl_3$): δ (ppm) = 181.81, 168.79, 167.18, 71.85, 71.53, 70.57, 70.53, 70.46, 70.38, 70.01, 69.94, 59.01, 57.41, 54.76, 44.68, 31.91, 31.07, 29.63, 29.59, 29.54, 29.50, 29.35, 29.29, 26.57, 26.07, 22.68, 14.13.

HRMS (ESI) *m/z*: $[M+H]^+$ calcd. for $C_{60}H_{112}N_5O_{14}$, 1126.82003; found, 1126.81981. LC-MS: t = 7.68 min, 1125.55 $[M]^+$.

Synthesis of 12c

11 (0.20 g, 0.54 mmol), **6** (0.29 g, 0.67 mmol) and K_2CO_3 (0.37 g, 2.69 mmol) were dissolved in dry CH_3CN (30 mL) and heated to reflux overnight. The solvent was removed by rotary evaporation and the reaction mixture was dissolved in CH_2Cl_2 (25 mL) and extracted with 1M NaOH (3 x 25 mL). The organic layers were collected and dried with $MgSO_4$, filtered, and concentrated in vacuum. The crude was purified by silica column chromatography (EtOAc/Pet ether: 10/90 – 60/40) to obtain the title product as a colorless oil.

Yield = 0.26 g, 66.3 %. ^{1}H NMR (300 MHz, $CDCl_3$): δ (ppm) = 7.38-7.30 (m, 10H), 5.08 (s, 4H), 3.67-3.63 (m, 16H), 3.59-3.57 (m, 4H), 3.48-3,45 (m, 2H), 3.42-3.36 (d, 3H), 3.26 (s, 2H), 2.60-2.45 (d, 4H), 1.58 (t, 2H), 1.27 (m, 16H). ^{13}C NMR (75 MHz, $CDCl_3$): δ (ppm) = 156.57, 136.64, 128.48, 128.02, 71.98, 71.52, 70.62, 70.59, 70.52, 70.06, 66.63, 58.99, 54.09, 53.50, 38.81, 29.64, 29.55, 29.47, 27.35, 26.09. HRMS (ESI) *m/z*: $[M+H]^+$ calcd. for $C_{39}H_{64}N_3O_9$, 718.46371; found, 718.46250. LC-MS: t = 6.49 min, 717.32 *m/z*: $[M]^+$.

Synthesis 3

Triethylsilane (4.0 mL, 25.21 mmol) was added dropwise to a stirring solution of **7c** (239 mg, 0.33 mmol) and palladium on carbon (80 mg, 0.72 mmol) in dry CH_3OH (10 mL) under a N_2 atmosphere and kept at RT overnight. The solution was filtered over celite, concentrated, and dissolved in $CHCl_3$ (50 mL). **1** (378.48 mg, 0.73 mmol) and DIPEA (0.26 mL, 1.47 mmol) were added to the reaction mixture and refluxed overnight. The solvent was removed by rotary evaporation and the residue was redissolved in CH_2Cl_2 (20 mL) and washed with 1M HCl (3 x 10 mL). The combined organic fractions were collected and dried with $MgSO_4$, filtered, and concentrated in a vacuum. The crude was purified by silica column chromatography (EtOAc: 100% - CH_3OH/CH_2Cl_2: 10/90) to obtain the final product as a yellow oil. The compound was further purified by HPLC and lyophilized to obtain a white solid.

Yield = 0.11 g, 21.5%. ^{1}H NMR (300 MHz, $CDCl_3$): δ (ppm) = 3.69-3.40 (m, 62H), 3.37 (s, 9H), 2.64 (s, 4H), 2.56 (s, 2H), 1.40 (m, 48H). ^{13}C NMR (75 MHz, $CDCl_3$): δ (ppm) = 185.16, 168.88, 167.07, 71.87, 71.52, 70.53, 70.49, 70.44, 70.36, 69.98, 69.93, 59.00, 44.66, 31.10, 29.61, 29.53, 29.31, 26.56, 26.08. HRMS (ESI) *m/z*: [M+H]+ calcd. for $C_{69}H_{130}N_5O_{19}$, 1332.93545; found, 1332.94272. LC-MS: t = 6.90 min, 1331.65 *m/z*: $[M]^+$.

Synthesis of 4

Tris(2-aminoethyl)amine (33.99 mg, 0.23 mmol), **1** (395.04 g, 0.77 mmol), and DIPEA (0.27 mL, 1.53 mmol) were dissolved in $CHCl_3$ (30 mL) and kept at reflux overnight. The solvent was removed by rotary evaporation and the residue was redissolved in CH_2Cl_2 (20 mL) and washed with 1M HCl (3 x 10 mL). The combined organic fractions were collected and dried with $MgSO_4$, filtered, and concentrated in vacuum. The crude was purified by silica column chromatography (EtOAc: 100% – CH_3OH/CH_2Cl_2: 10/90) to obtain the final product as a yellow solid. The compound was further purified by HPLC and lyophilized to obtain a white solid.

Yield = 0.131 g, 86.9%.^{1}H NMR (300 MHz, $CDCl_3$): δ (ppm) = 7.65 (s, 4H), 3.72-3.60 (m, 60H), 3.59-3.45 (m, 6H), 3.37 (s, 9H), 2.62 (s, 6H), 1.64-1.53 (m, 12H), 1.39-1.29 (m, 6H), 1.25 (s, 30H). ^{13}C NMR (75 MHz, $CDCl_3$): δ (ppm) = 182.66, 168.50, 167.17, 71.66, 71.52, 70.31, 70.19, 70.16, 70.11, 70.04,

69.71, 59.01, 56.69, 55.65, 44.50, 31.08, 29.51, 29.44, 29.24, 26.46, 25.96. HRMS (ESI) *m/z*: $[M+H]^+$ calcd. for $C_{75}H_{136}N_7O_{21}$, 1470.97838; found, 1470.97865. LC-MS: t = 6.96 min, 1469.76 *m/z*: $[M]^+$.

Gel inversion test

The critical gelation concentration (CGC) is defined as the minimum concentration of a given compound to form a hydrogel. A concentration series of **2-5** were prepared with H_2O in 2 mL glass vials before sonicating for 20 minutes. All the samples were left to equilibrate overnight prior to imaging the inverted vials. All hydrogels for the following tests were prepared in H_2O.

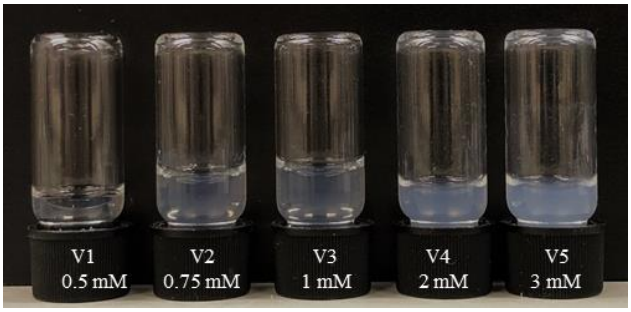

Figure S6. Gel inversion test of **2** in H_2O at various concentration of 0.5 mM (V1), 0.75 mM (V2), 1 mM (V3), 2.0 mM (V4) and 3.0 mM (V5) in glass vials.

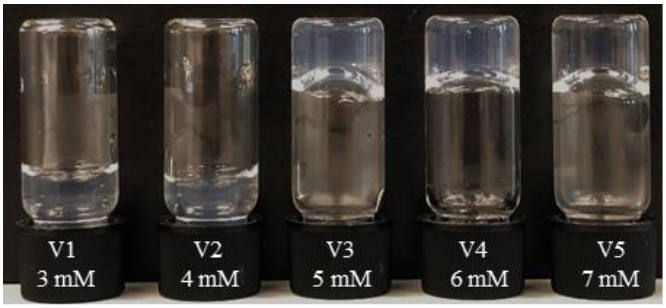

Figure S7. Gel inversion test of **3** in H_2O at concentration 3.0 mM (V1), 4.0 mM (V2), 5.0 mM (V3), 6.0 mM (V4) and 7.0 mM (V5) in glass vials.

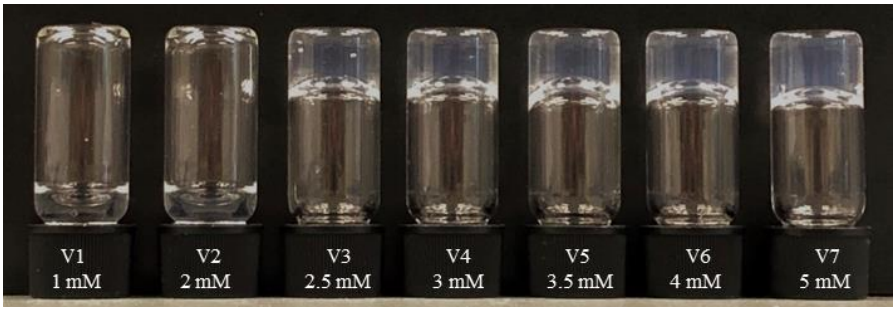

Figure S8. Gel inversion test of **4** in H_2O at concentration 1.0 mM (V1), 2.0 mM (V2), 2.5 mM (V3), 3.0 mM (V4), 3.5 mM (V5), 4.0 mM (V6) and 5.0 mM (V7) in glass vials.

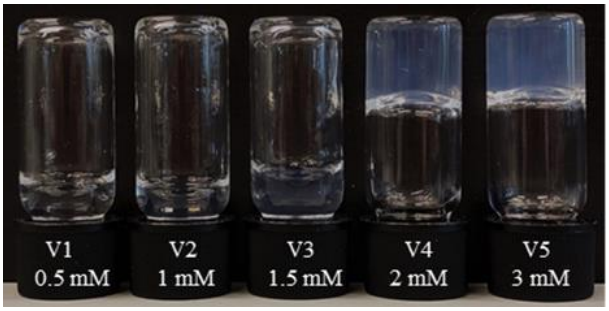

Figure S9. Gel inversion test of **5** in H_2O at concentration 0.5 mM (V1), 1.0 mM (V2), 1.5 mM (V3), 2.0 mM (V4) and 3.0 mM (V5) in glass vials.

Oscillatory rheology

Hydrogels of **3-5** (5 mM) were prepared as described above. Time sweep measurements were performed at a strain amplitude (γ) of 0.05% and at a frequency (ƒ) of 1 Hz. Strain sweeps were conducted in a range of strain amplitudes of 0.01 - 500% at a fixed frequency (ƒ=1 Hz). Frequency sweeps were executed over a frequency range from 0.01 - 3 Hz at a constant strain amplitude (γ=0.05%). A step-strain measurement was performed to estimate the self-recovery of the hydrogel. The measurement started with a time sweep (3600 s, f = 1.0 Hz, γ = 0.05%) and was followed by a frequency sweep (ƒ = 0.01 - 3 Hz, γ = 0.05%). Once a plateau in the storage modulus (G') was reached, a strain of 300% was applied to the sample for 120 s and was then left to recover while measuring at a low strain percentage (ƒ = 1 Hz, γ = 0.05%) for 800s. The process was repeated in this manner for two cycles. Temperature sweep tests were performed by applying a temperature ramp at 0.1 °C/min between 25 to 85°C under a fixed strain (γ = 0.05%) and frequency (ƒ = 1 Hz) with mineral oil placed around the geometry to prevent the drying of the hydrogels during the experiment. Storage modulus (G') and loss moduli (G'') were recorded during the process.

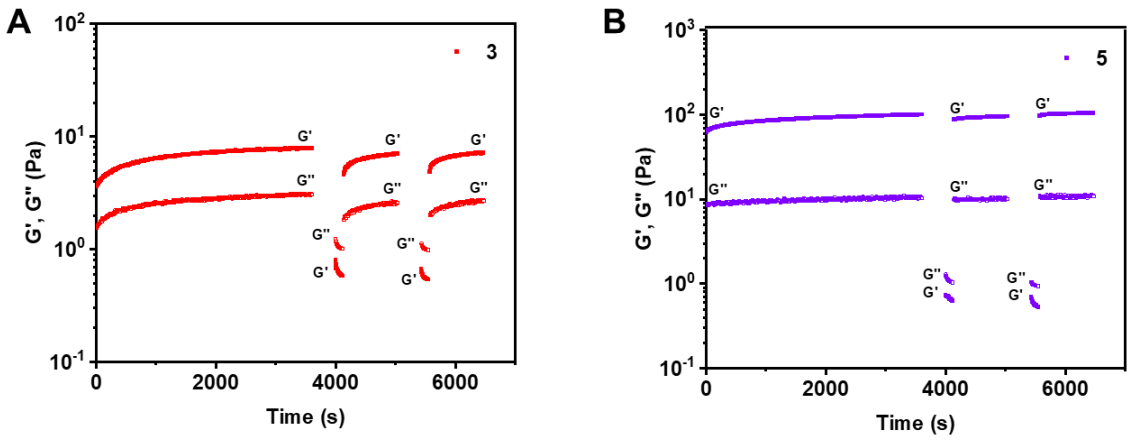

Figure S10. Time sweep measurements (ƒ = 1 Hz, γ = 0.05%) and self-recovery process of hydrogels **3** (A) and **5** (B) (5 mM) in H_2O at 25 °C. The absence of data before the application of high strain is due to the acquisition of a frequency sweep (ƒ = 0.01 to 3 Hz, γ = 0.05%).

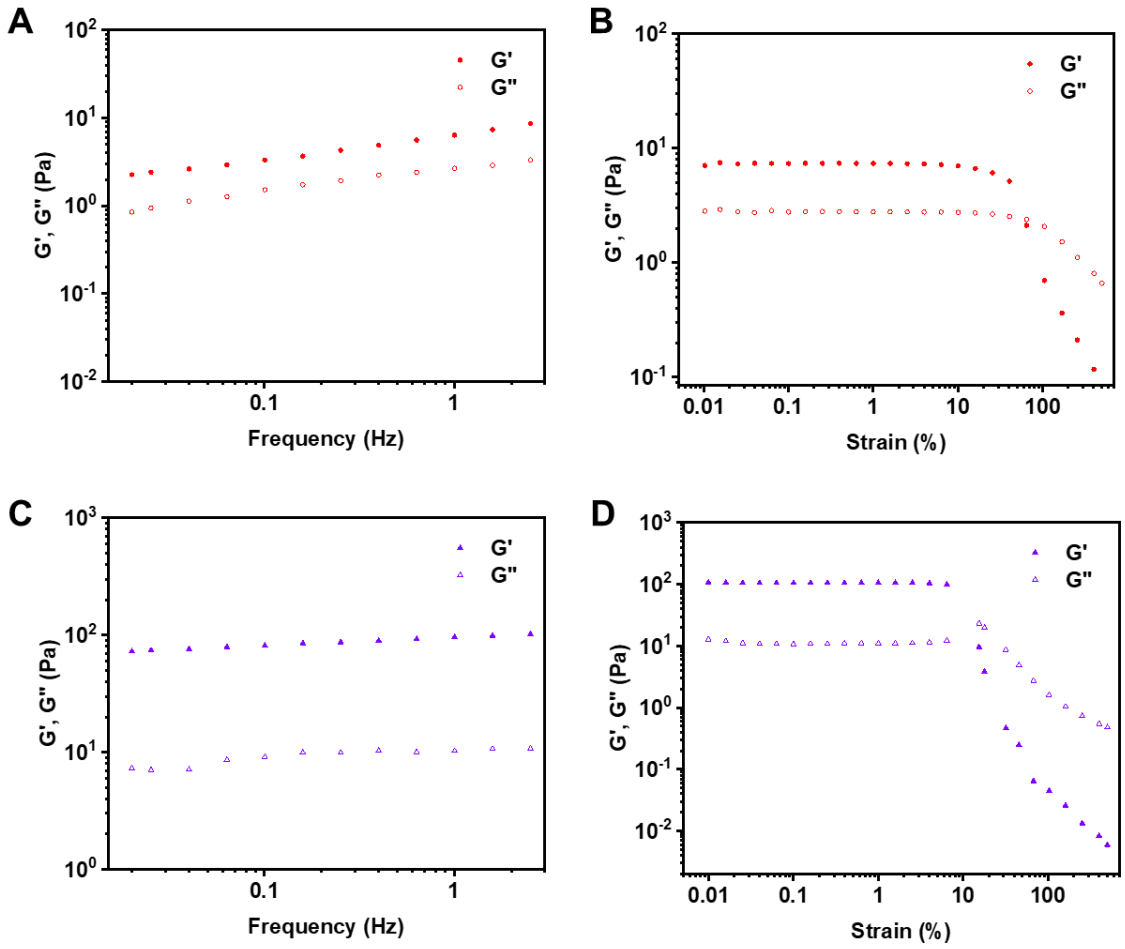

Figure S11. Oscillatory rheology measurements of hydrogels **3** and **5** (5 mM) in H_2O at 25 °C: Amplitude sweep (ƒ = 1 Hz) for hydrogels **3** (B) and **5** (D). Frequency sweep (γ = 0.05% strain) of hydrogels **3** (A) and **5** (C).

Cryogenic Transmission Electron microscopy (cryo-TEM)

Hydrogels (5 mM) of **3**-**5** were prepared as described before and diluted to the imaging concentration (0.5 mM). Subsequently, the samples (3 µL, 0.5 mM) were applied to a freshly glow-discharged carbon 200 mesh Cu grid. The excess liquid was blotted off (3 s) at 100% humidity and plunge-frozen in liquid ethane using a Vitrobot plunge-freezer. The images were recorded on a BM-Ceta (4k x 4k) at a nominal magnification of 73000x (1.34 Ångstrom per pixel) and defocus of -2.0 to -3.0 µm. The length and width of the fibers were measured using Fiji software. The size distribution was obtained by measuring the length and the width of at least 50 fibers per sample.

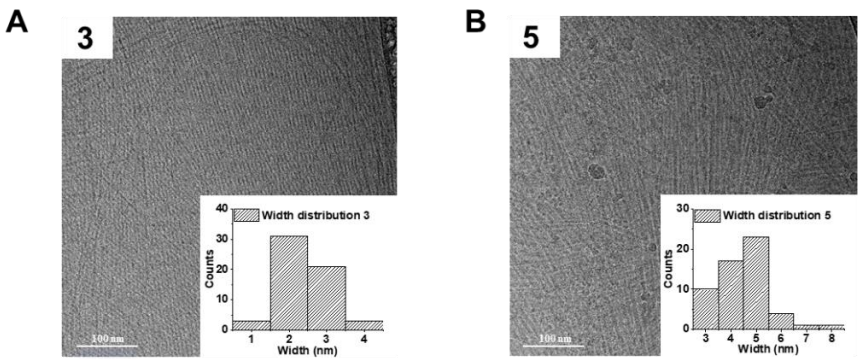

Figure S12. Cryo-TEM images of (A) **3** and (B) **5** at (0.5 mM in H_2O). Insert: Histograms of fiber width distribution for a sample size of N ⩾ 50. Scale bar: *100 nm*.

Atomic force microscopy (AFM)

Compounds **1-5** were dissolved in H_2O (0.25 mM) and equilibrated overnight. The samples were prepared by dropping solutions (10 µL) on a 1 cm^{-2} piece of mica with spin coating (2 min, 2000 rpm). The samples were dried overnight at RT prior to imaging. The obtained images were processed using the Nanoscope software.

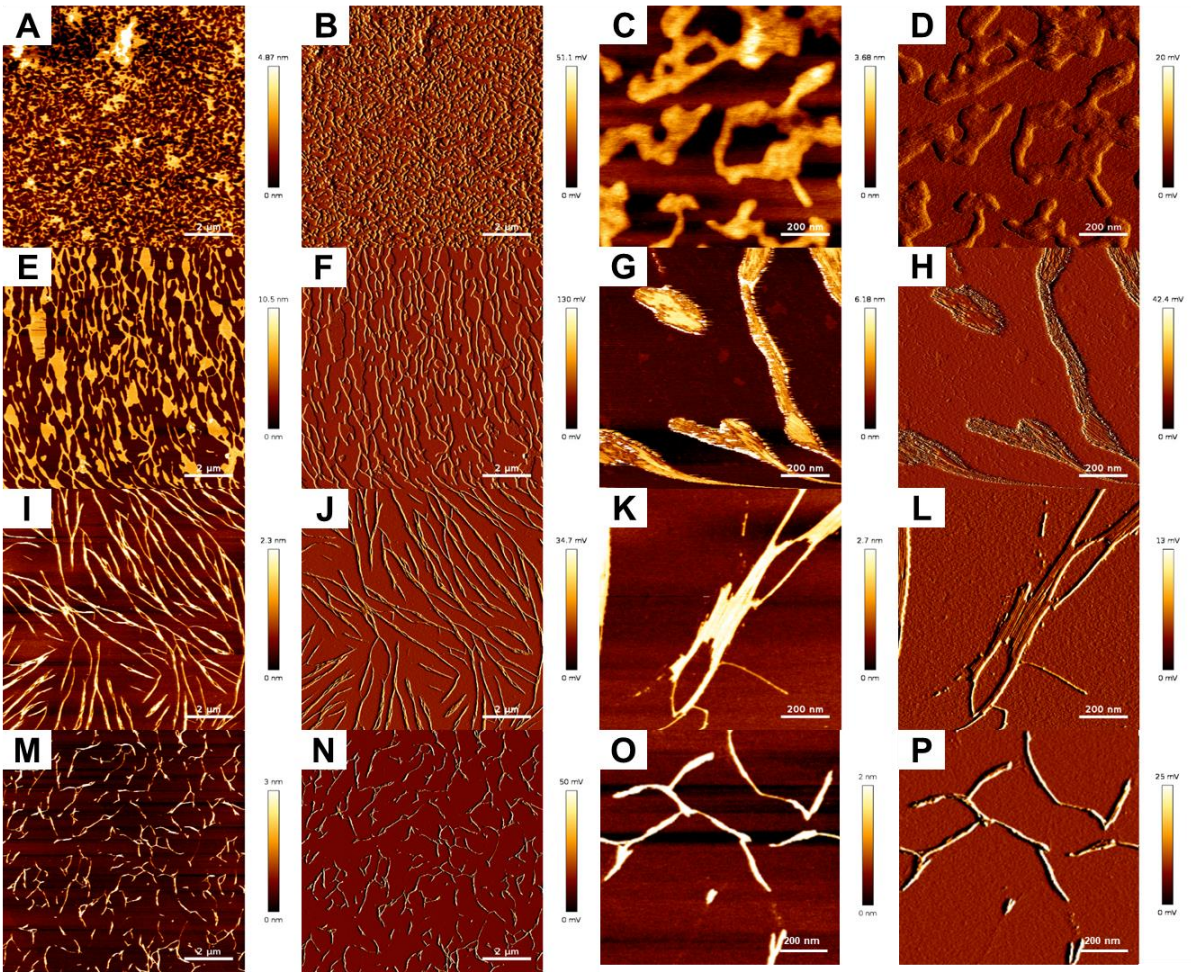

Figure S13. AFM height and amplitude phase images of **2-5** by spinning coating and deposited on mica overnight after dissolution. AFM height images at low magnification: (A) **2**, (B) **3**, (C) **4**, (D) **5**. Scale bar: *2 µm.* AFM phase images at low magnification: (E) **2**, (F) **3**, (G) **4**, (H) **5**. Scale bar: *2 µm.* AFM height images at high magnification: (I) **2**, (J) **3**, (K) **4**, (L) **5**. Scale bar: *200 nm*. AFM phase images at high magnification: (M) **2**, (N) **3**, (O) **4**, (P) **5**. Scale bar: *200 nm.*

Small angle X-ray scattering (SAXS)

Samples **3**-**5** (2 mg/mL) were prepared in H_2O before measurement as previously described and pipetted into 2 mm quartz capillaries before the measurements. The SAXS patterns were adjusted utilizing the calibrated detector response function to establish an absolute intensity scale, along with known sample-to-detector distance, measured incident, and transmitted beam intensities. These patterns were then azimuthally averaged, yielding one-dimensional SAXS profiles. To isolate the scattering curves specific to the self-assembled fibers, the scattering contribution of the solvent and quartz cell was subtracted using the SAXS utilities within the software package available at http://www.sztucki.de/SAXSutilities/. The resulting SAXS profiles were further analyzed using the software package SASview, accessible at http://www.sasview.org/.

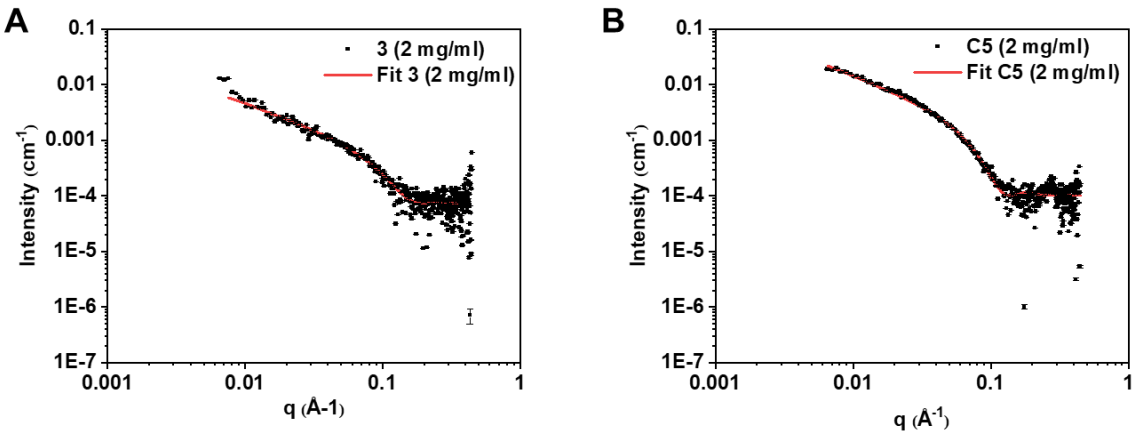

Figure S14. Small-angle X-ray scattering profiles of fibers (A) **3** and (B) **5** collected at a concentration of 2 mg/mL. Black dots represent experimental data; red line represents fit with a form factor for flexible cylinders.

UV-Vis spectroscopy

Stock solutions of **1-5** (1 mM) were prepared with H_2O in glass vials (2 mL) and subsequently diluted to the measured concentrations or solvent mixtures. The individual samples were left to equilibrate overnight at RT prior to UV-Vis measurements.

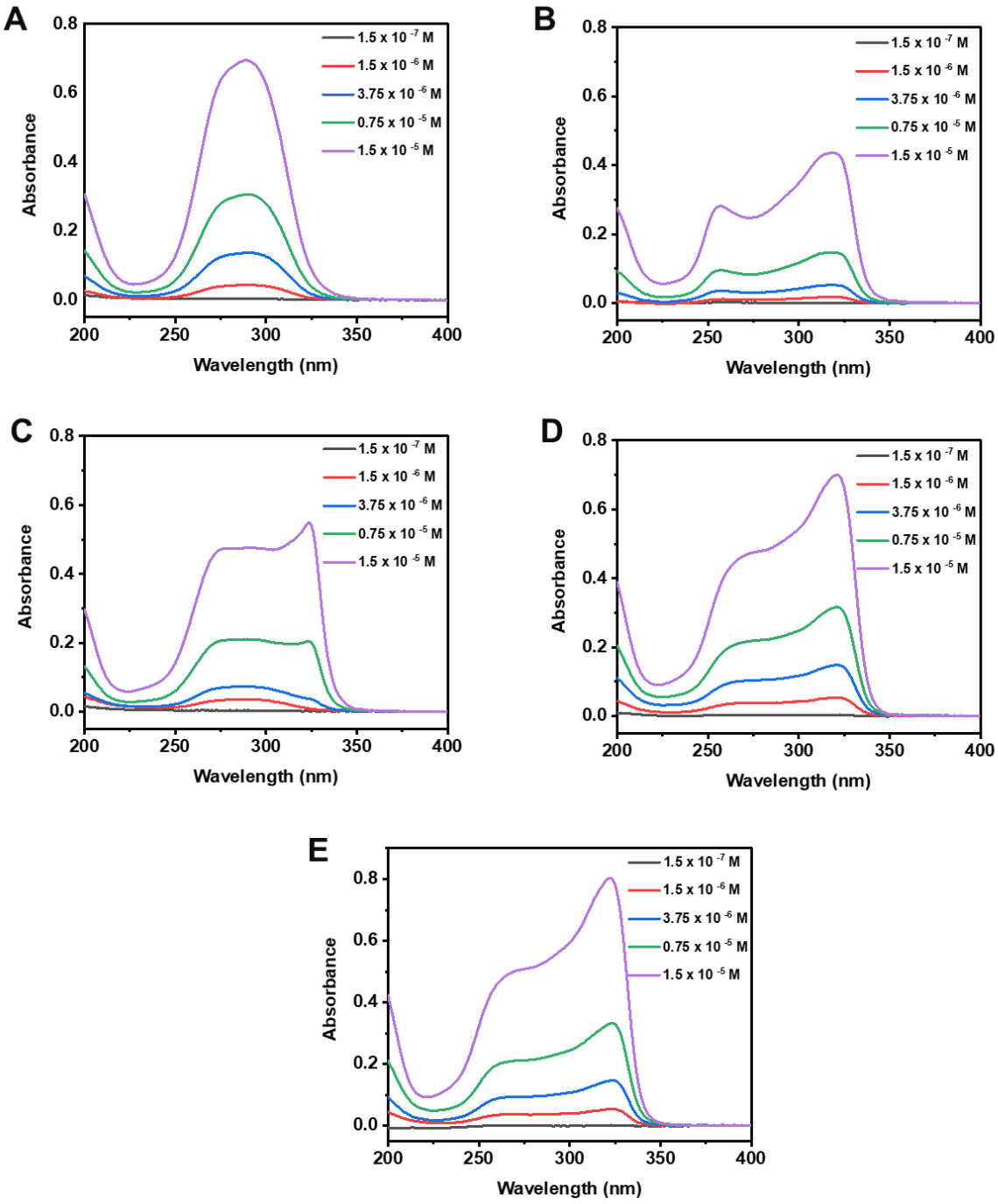

Figure S15. Concentration-dependent UV-Vis spectra of **1** (A), **2** (B), **3** (C), **4** (D) and **5** (E) in H_2O.

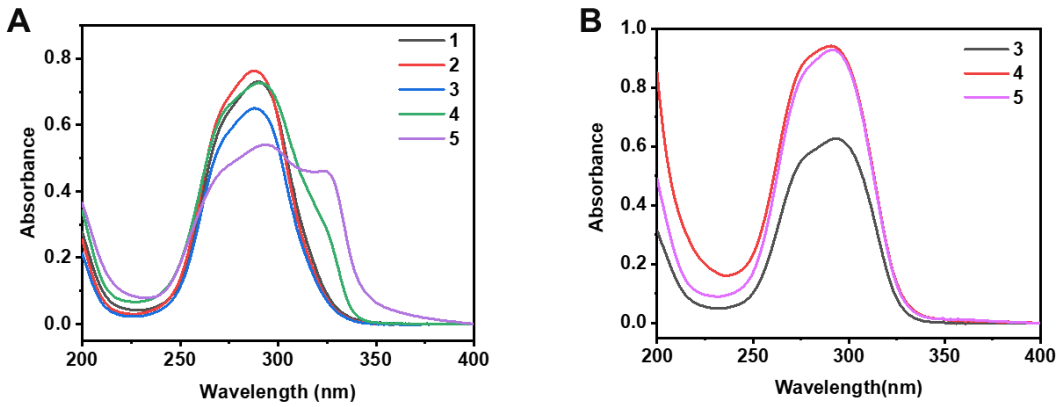

Figure S16. UV-Vis spectra of (A) **1-5** (1.5×10^{-5} M) in CH_3CN and (B) **3-5** in CH_3CN-H_2O (v/v, 6:4).

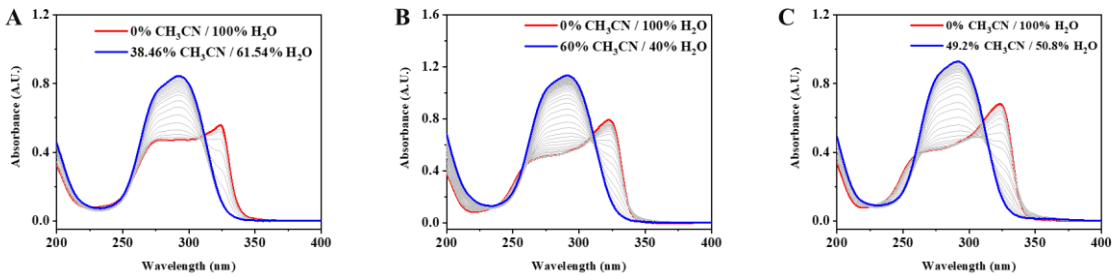

Figure S17. UV-Vis titration spectra of 3-5 (1.5×10^{-5} M) in CH_3CN and in CH_3CN-H_2O (v/v, 6:4). (A) **3**, (B) **4**, (C) **5**.

Fluorescence spectroscopy

Stock solutions of **1-5** (1 mM) were prepared in H_2O by sonication for 20 min, diluted to the desired concentration (1.5×10^{-5} M) and left to equilibrate overnight at RT prior to measurement. A Nile red dye solution (5×10^{-3} mg/mL) was prepared in methanol before being pipetted (12 µL) into the individual wells of a black 96-well plate. The methanol was removed in a vacuum oven at 25°C for 4 hours. Subsequently, an aliquot (200 µL) from the stock solutions of **1-5** was pipetted into a 96-well plate containing the Nile red dye and equilibrated overnight before measurement. An excitation wavelength of 520 nm was used and emission data was recorded from 575 to 750 nm. The Nile red dye in H_2O (200 µL) was also measured as a negative control.

Fourier Transform Infrared (FTIR) Spectroscopy

Compounds **2-5** were prepared in H_2O (200 µL, 8 mM) as previously described and left to equilibrate overnight at RT. The samples were then lyophilized prior to the acquisition of FTIR spectra.

A liquid transmission cell consisting of CaF_2 windows was cleaned carefully with D_2O or CD_3CN before use. Compounds **3-5** (500 µL, 5 mM) were first sonicated in D_2O for 20 min and then lyophilized. This process was repeated 3 times to remove traces of H_2O from the samples. **3-5** (5 mM) were then prepared in D_2O and 4:6 D_2O/CD_3CN individually by sonication for 20 min. The samples were sealed and left to equilibrate overnight at RT prior to measurement. The recorded IR spectra were plotted with respect to absorbance and appropriate background subtracted.

Table S1 Infrared spectrum assignment of vibrational modes from 3500-1500 cm^{-1} for the various peaks indicated in Figure 2D of freeze-dried samples **2-5**.

	2	**3**	**4**	**5**
v (N-H)	3166 cm^{-1} (squaramide)	3169 cm^{-1} (squaramide)	3165 cm^{-1} (squaramide)	3315 cm^{-1} (carbamate) 3164 cm^{-1} (squaramide)
v (C-H)	2920 cm^{-1} (antisym) 2852 cm^{-1} (sym)	2924 cm^{-1} (antisym) 2855 cm^{-1} (sym)	2923 cm^{-1} (antisym) 2854 cm^{-1} (sym)	2918 cm^{-1} (antisym) 2851 cm^{-1} (sym)
Ring Breathing	1797 cm^{-1}	1799 cm^{-1}	1799 cm^{-1}	1799 cm^{-1}
v (C=O)	1654 and 1639 cm^{-1} (squaramide)	1654 and 1639 cm^{-1} (squaramide)	1654 and 1639 cm^{-1} (squaramide)	1719 and 1689 cm^{-1} (carbamate) 1654 and 1639 cm^{-1} (squaramide)

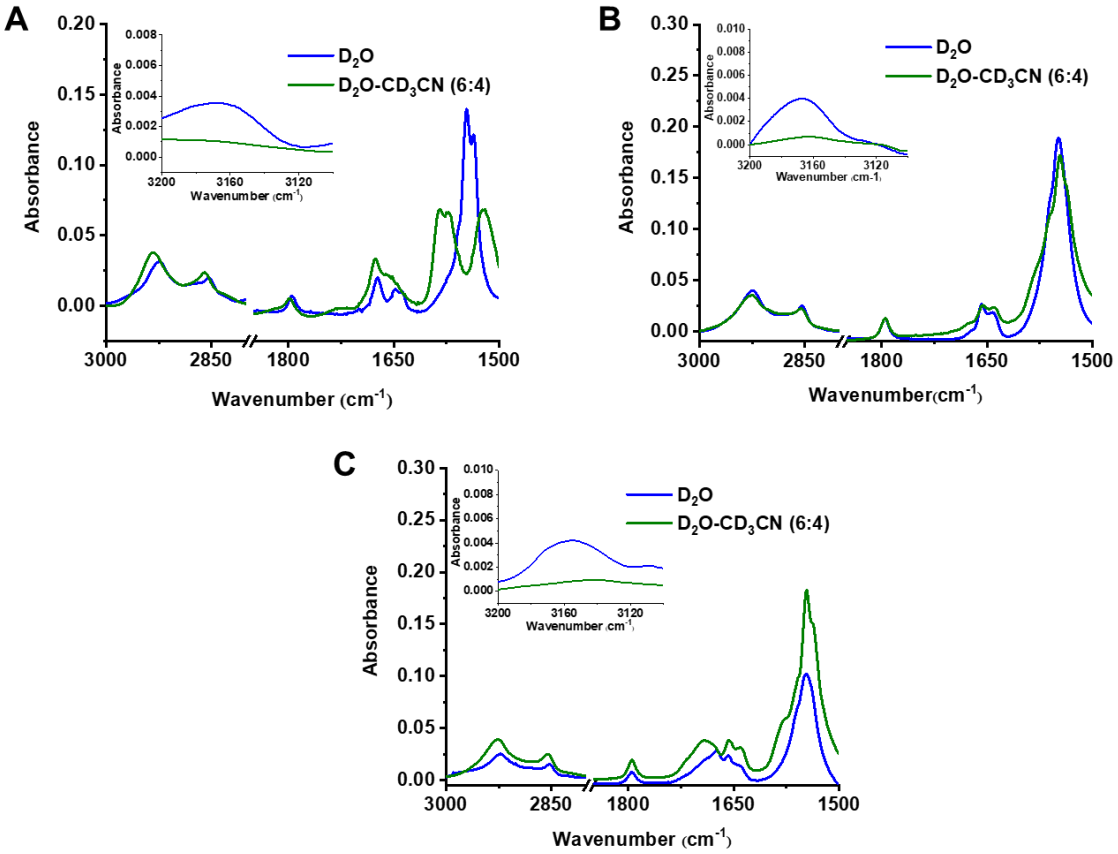

Figure S18. IR spectrum recorded in the N-H region (inset), amide I and amide II regions in D_2O and CD_3CN-D_2O (v/v, 6:4) at 5 mM for **3** (A),**4** (B) and **5** (C).

Table S2 Infrared spectrum assignment of vibrational modes from 3000-1500 cm^{-1} for the various peaks indicated in Figure **S18** of **3-5** in self-assembly state and monomer state.

	3		**4**		**5**	
	D_2O	**D_2O-CD_3CN (v/v, 6:4)**	**D_2O**	**D_2O-CD_3CN (v/v, 6:4)**	**D_2O**	**D_2O-CD_3CN (v/v, 6:4)**
v (N-H)	3174 cm^{-1} (squaramide)	3170 cm^{-1} (squaramide)	3166 cm^{-1} (squaramide)	3162 cm^{-1} (squaramide)	3155 cm^{-1} (squaramide)	3140 cm^{-1} (squaramide)
v (C-H)	2923 cm^{-1} (antisym) 2854 cm^{-1} (sym)	2933 cm^{-1} (antisym) 2860 cm^{-1} (sym)	2924 cm^{-1} (antisym) 2854 cm^{-1} (sym)	2926 cm^{-1} (antisym) 2855 cm^{-1} (sym)	2923 cm^{-1} (antisym) 2853 cm^{-1} (sym)	2926 cm^{-1} (antisym) 2855 cm^{-1} (sym)
Ring Breathing	1795 cm^{-1}	1798 cm^{-1}	1795 cm^{-1}	1795 cm^{-1}	1795 cm^{-1}	1794 cm^{-1}
v (C=O)	1648 cm^{-1}, 1638 cm^{-1} (squaramide)	1652 cm^{-1}, 1635 cm^{-1} (squaramide)	1658 cm^{-1}, 1642 cm^{-1} (squaramide)	1656 cm^{-1}, 1640 cm^{-1} (squaramide)	1674 cm^{-1} (carbamate) 1658 cm^{-1}, 1642 cm^{-1} (squaramide)	1692 cm^{-1} (carbamate) 1657 cm^{-1}, 1641 cm^{-1} (squaramide)

Lower critical solution temperature (LCST) measurements

Samples of **3-5** (0.2 mM and 1 mM) in H_2O were prepared as previously described and equilibrated overnight prior to measurement. Samples (2 mL) were placed into UV cuvettes, equilibrated at 20°C for 10 minutes before heating at 0.1°C / min to 90°C. The cuvettes were sealed with high-temperature-resistant tape to prevent evaporation.

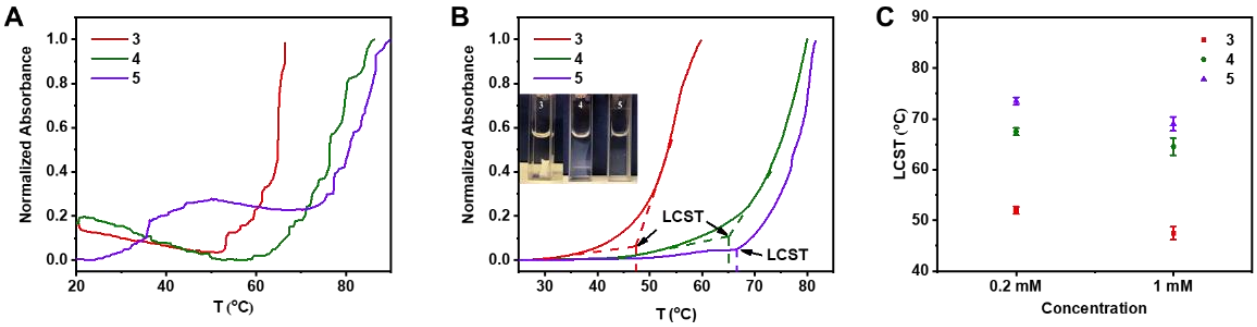

Figure S19. Turbidity measurements from UV-Vis absorbance spectra at 450 nm of **3-5** with increasing temperature from 20°C to 90°C at 0.1°C/min: (A) 0.2 mM; (B) 1 mM (Insert: digital picture of **3-5** after the test and cooled back to RT). (C) LCST of **3-5** at 0.2 mM and 1mM.

Differential scanning calorimetry (DSC) measurements

Hydrogels of **3-5** (5 mM) in H_2O were prepared as previously described and equilibrated overnight prior to measurement. Hydrogels (200 µL) were first placed into platinum capillary tubes, for every experiment, the samples were cooled to 0°C and equilibrated for 10 minutes before heating at 2°C / min to130°C under N_2 flow, followed by a cooling process at the same speed. The thermograms recorded were analyzed with the NanoAnalyze 2.0 software. T_1 and T_2 was determined as the peak1 and peak2 temperature values, ΔH corresponded to enthalpy and ΔS corresponded to entropy. The H_2O baseline underwent a minimum of 5 heating/cooling cycles until consistent heating was achieved, subsequently, it was subtracted from the sample data.

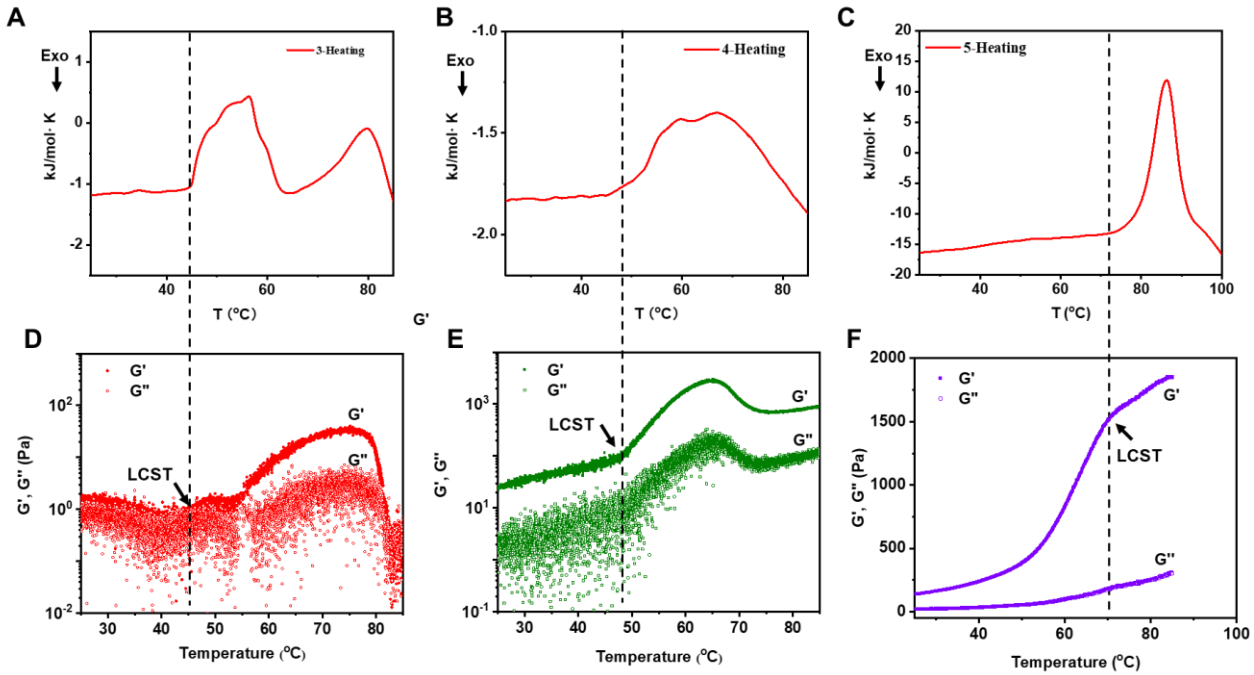

Figure S20. DSC curves measured for hydrogels of **3-5** (5 mM) heating from 20°C to 100°C: (A) **3**, (B) **4**, (C) **5**. Temperature sweeps for hydrogels (5 mM) (D) **3**, (E) **4** and (F) **5** in H_2O heating 20°C to 85°C at a rate of 0.1°C/min.

Hydrogel heating process

Hydrogels of **3-5** (5mM) were prepared as previously described and equilibrated overnight prior to the heating experiment. The hydrogels were put into NMR tubes and heated from RT to 130°C at a rate of ~2°C / min and then cooled back to RT. The heating process was imaged using a digital camera at different time points.

Polarized optical microscopy (POM)

Hydrogels of **3-5** (5 mM, 200 µL) were prepared, heated in NMR tubes and cooled down to RT as described before. The samples (100 µL) were carefully drop-casted onto a glass slide before imaging.

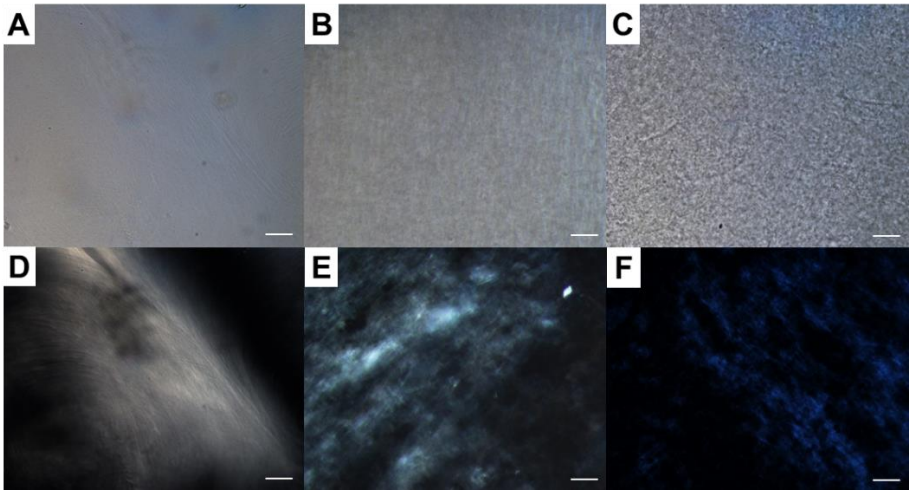

Figure S21. Optical and polarized optical microscopy (POM) images of squaramide-based hydrogels **3-5** (5 mM): (A) **3**, (B) **4,** (C) **5** in optical mode. (D) **3**, (E) **4,** (F) **5** in polarized mode. Scale bar: *100µm*.

Scanning electron microscopy (SEM)

The surface morphology of the heated hydrogels of **3-5** and **3'-5'** were examined by SEM. Samples of **3'-5'** (5 mM, 500 µL) were prepared, heated in NMR tubes, and cooled down to RT as described before. Afterwards, each sample (100 µL) was drop-casted on a desiccator with double-sided carbon tape on it, and dried in a 25°C vacuum overnight. The samples were sputter-coated with 2 mm gold–palladium (Au/Pd) prior to SEM imaging.

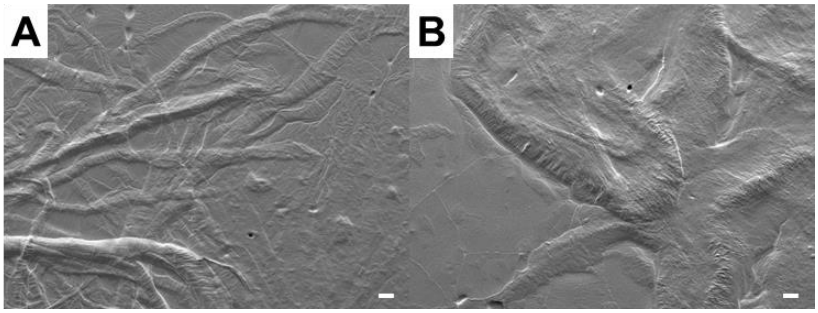

Figure S22. SEM pictures of hydrogels (5 mM) after heating process: (A) **4'**, (B) **5'**. Scale bar: *100µm*.

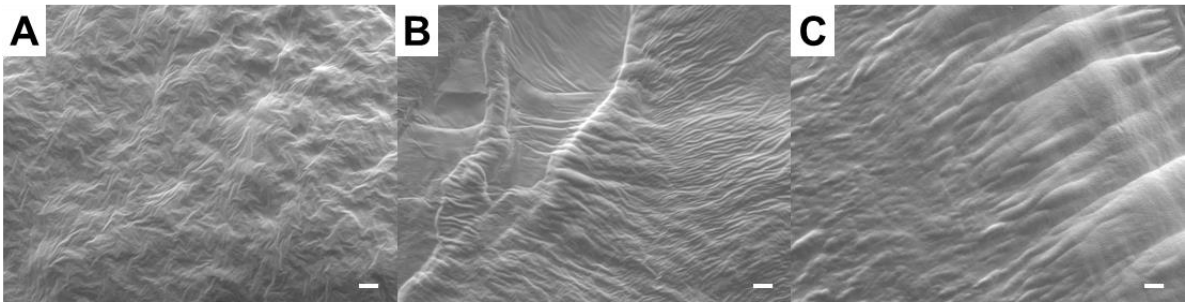

Figure S23. SEM pictures of hydrogels **3'-5'** (5 mM) after heating process: (A) **3**. (B) **4**. (C) **5**. Scale bar: *10µm.*

X-ray diffraction analysis (XRD)

Hydrogels of **3-5** (5 mM, 500 µL) were prepared, heated in NMR tubes, and cooled down to RT as described before. Afterwards, samples were lyophilized and directly loaded onto a rectangular glass sample holder, and then scans were carried out immediately and after prescribed times at a scan rate of 0.5°/min. Samples without heating process were lyophilized and measured in the same manner.

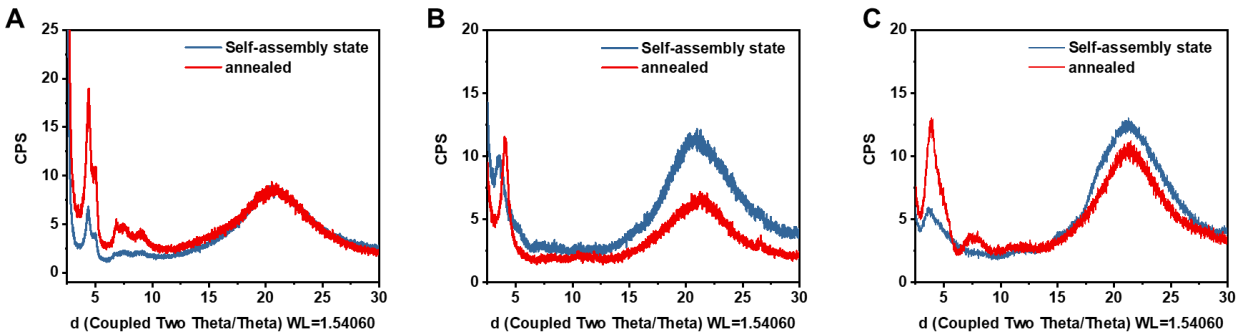

Figure S24. XRD of lyophilized hydrogels **3**-**5** and their heated samples **3'**-**5'**. (A) **3** and **3'**. (B) **4** and **4'**. (C) **5** and **5'**.

Reference

(1) Tong, C.; Liu, T.; Saez Talens, V.; Noteborn, W. E. M.; Sharp, T. H.; Hendrix, M.; Voets, I. K.; Mummery, C. L.; Orlova, V. V.; Kieltyka, R. E. Squaramide-Based Supramolecular Materials for Three-Dimensional Cell Culture of Human Induced Pluripotent Stem Cells and Their Derivatives. Biomacromolecules 2018, 19 (4), 1091.